*J. Fluid Mech.* (2006), *vol.* 569, *pp.* 209–247.  
doi:10.1017/S002211200600262X Printed in the United Kingdom

# Direct numerical simulation of flow and heat transfer in a turbine cascade with incoming wakes

By JAN G. WISSINK AND WOLFGANG RODI

Institute for Hydromechanics, University of Karlsruhe, Kaiserstr. 12, D-76128 Karlsruhe, Germany

(Received 1 August 2005 and in revised form 6 June 2006)

Direct numerical simulations (DNS) of flow in a turbine cascade with heat transfer have been performed. The set-up of the simulations was chosen in close accordance with previous experiments. Three of the experimental situations were simulated: one without free-stream turbulence and two with periodically incoming wakes of different frequency and with different levels of background fluctuation. Hence, the calculations allow us to study the influence of impinging wakes and background fluctuations on the development of the boundary layers and the local Nusselt number along the surfaces of the heated blade. Along the suction side, the pressure gradient is first favourable and then turns adverse near the trailing edge and the boundary layer remains laminar for the case without free-stream turbulence with the Nusselt number showing the typical decay from the leading to the trailing edge. With periodic wakes and background turbulence, transition occurs when the pressure gradient turns adverse, but intermittency persists so that the boundary layer is not fully turbulent when the trailing edge is reached. In this region, the heat transfer is increased significantly by an amount comparable to that found in the experiments. In the pre-transitional region with favourable pressure gradient, the flow acceleration stretches the free-stream vortices, aligning their axis with the flow direction, thereby forming streamwise vortical structures. These increase the laminar heat transfer in this region by 20–30 %, which is, however, much less than observed in the experiments. On the pressure side, the pressure gradient is favourable along the entire blade so that the boundary layer remains laminar. Here, the wakes, through their impingement, also generate streamwise vortical structures which, because of the low convection speed on this side, have a very long lifetime compared to the structures along the suction side. Also these structures increase the laminar heat transfer by about 30 %, which for the case with the highest wake frequency is again much less than in the experiments. The simulated average level of fluctuations in the laminar parts of the boundary layers is comparable or even higher than that in the experiments so that it seems likely that a difference in the spectral contents causes the discrepancies. The wake turbulence entering the calculation domain corresponds to that in far wakes with relatively small-scale structures, whereas in the experiments the wakes most probably still carried some large-scale fluctuations of the size of the wake width, which have been found to be more effective in increasing laminar heat transfer.

## 1. Introduction

The boundary-layer flow around turbine blades is very complex as unsteady wakes, generated by an upstream row of blades, pass through the cascade channels and

have a great influence on the flow field and the heat transfer to the blades. Along the suction side, the streamwise pressure gradient usually turns from favourable near the leading edge to adverse near the trailing edge, giving rise there to various possible boundary-layer transition scenarios, of which bypass transition and separation-induced transition are the most common. On this side, the periodically impinging wakes cause the location of transition to alternately move upstream and downstream. Also, both uniform 'background' disturbances, which are mostly present, and the concentrated free-stream disturbances carried in the wakes may completely or intermittently suppress separation of the suction-side boundary-layer in the adverse pressure gradient (APG) region. Both flow separation and transition to turbulence are known to have a significant effect on the heat transfer. Along the entire pressure side, the streamwise pressure gradient is usually favourable so that the boundary layer mostly remains laminar. Here the impinging wakes lead to the formation of longitudinal vortical structures which typically have a long lifetime. Experiments have further shown that the impinging free-stream disturbances may cause a significant increase in heat transfer despite the boundary layer remaining laminar on the pressure side, and a similar influence was also found in the pre-transitional, still laminar part of the boundary layer on the suction side.

For the optimization of the blade design, and especially the efficient cooling of the blades, reliable prediction methods for the flow and heat transfer are required that can account realistically for the unsteady effects. So far, mainly unsteady Reynolds averaged Navier–Stokes (URANS) solvers are used to calculate the flow and heat transfer in turbine cascades, see for instance, Cho *et al.* (1993); Edmunds *et al.* (1999); Michelassi *et al.* (1999); Hummel (2002) and Lardeau & Leschziner (2004). It has been found, however, that the models available have difficulty in simulating realistically the complex phenomena described above. To be able to improve these models, both an understanding of the underlying physical mechanisms and the availability of high-quality data for testing these models are required. In the past, the only possibility of achieving these goals was to perform experiments, which, however, gave only limited information on the complex transition and heat transfer phenomena. Examples of such experiments can be found in, for instance, Liu & Rodi (1991), who performed experiments of wakes impinging on a flat-plate boundary-layer and Dullenkopf, Schulz & Wittig (1991), Liu & Rodi (1994*a*, *b*), Schobeiri, Pappu & Wright (1995), Schulte & Hodson (1998) and Stadtmüller & Fottner (2001) who performed experiments of flow around turbine blade models.

Because of recent increases in computational power, it is possible to perform large-eddy simulations (LES) and direct numerical simulations (DNS) of the relatively low-Reynolds-number flow in a low-pressure turbine (LPT) cascade. DNS is an ideal tool for studying complex flow phenomena without having to resort to model assumptions, while it also provides detailed data for the development and improvement of turbulence models. LES of flow in LPT cascades has been performed by, for instance, Michelassi, Wissink & Rodi (2002) and Raverdy *et al.* (2003). The first DNS of a turbine-related flow problem was performed by Wu *et al.* (1999), who chose the set-up of their computation in accordance with experiments performed by Liu & Rodi (1991). In this DNS, the effect of impinging wakes on a flat-plate boundary layer was studied. Wake disturbances superposed on the inlet boundary-layer profile were found to evolve quickly into longitudinal puffs. These puffs were selectively intensified by interaction of the boundary layer with certain types of turbulent eddies from the free-stream wakes through a localized instability. Eventually, this was followed

by a breakdown of the puffs into young turbulent spots, which broaden and finally amalgamate downstream.

In a subsequent DNS, Wu & Durbin (2001) simulated the flow in the T106 cascade with periodically incoming wakes. In this DNS they found that the wakes are passively convected by the free stream. As also observed in the DNS of separating flow in a T106 cascade at a lower Reynolds number performed by Wissink (2003), the impinging wakes induce the formation of longitudinal vortices along the pressure side of the turbine blade. In the centre of the passage between the blades, the wake is severely deformed as a result of straining and stretching by the free-stream flow. At the apex of the deformed wake, the direction of compression is aligned with the axis of the wake, which is similar to 'Case C' in Rogers (2002), and was found to result in the production of turbulent kinetic energy. Rogers studied the effects of mean strain applied to a self-similar turbulent plane wake. He discovered that when the direction of compression is parallel to the axis – or centreline – of the wake (Case C), production of normal stresses and of shear stress $\overline{u'v'}$ occurs, the former of which contributes to the turbulent kinetic energy. Along the suction side of the blade, Wu & Durbin (2001) reported the appearance of turbulent spots triggered inside the boundary-layer flow at mid-chord by impinging wakes. These turbulent spots were found to merge downstream into the fully turbulent region at the trailing edge.

In the DNS of Wissink (2003) of flow in the T106 cascade, because of the combination of a relatively large inflow angle and a low Reynolds number, the boundary layer along the suction side of the blade was found to separate. The separated boundary layer was found to roll-up because of a Kelvin–Helmholtz instability, whereas production of kinetic energy was concentrated inside the rolls of re-circulating flow. Because of the presence of periodically impinging wakes, separation was intermittently suppressed.

In the DNS of Kalitzin, Wu & Durbin (2003), flow in a T106 turbine cascade with incoming uniformly distributed free-stream disturbances was studied. With a turbulence level of $Tu = 5\,\%$ at the inlet, they observed by-pass transition in the adverse-pressure-gradient region of the suction-side boundary-layer somewhat upstream of the trailing edge. Compared to the incoming wakes in the simulation of Wu & Durbin (2001), the uniformly distributed disturbances were found to be less effective in triggering boundary-layer instabilities.

In a DNS of a transitional flat-plate boundary-layer with periodically incoming wakes, Wu & Durbin (2000) included passive heat transfer by fixing the temperature of the slightly heated flat plate. Their results show a strong correlation between local increases in heat transfer and the presence of boundary-layer fluctuations in, for instance, turbulent spots or the fully turbulent boundary layer farther downstream.

In experimental studies of 'laminar' heat transfer – that is: the heat transfer in regions where the boundary layer is laminar – along a flat plate affected by free-stream fluctuations, Kestin, Maeder & Wang (1961) and Junkhan & Serovy (1967) discovered that in, order for these fluctuations to be able to increase heat transfer, the laminar boundary-layer flow must be accelerating. This finding was confirmed by the experiments of Schulz (see Wittig *et al.* 1985), who measured the heat transfer distributions around a typical fore-loaded airfoil for several free-stream turbulence levels. Along the stagnation region at the leading edge, where the acceleration is very strong, the highest heat transfer was found. The main effect on the suction surface, where a laminar to turbulent transition occurs, was to cause an earlier onset of transition which in turn induced an earlier increase in heat transfer. Along the

pressure surface, where the highly accelerated boundary-layer remains laminar, the main effect of turbulence was to cause a large increase in laminar heat transfer. In earlier experiments, Yardi & Sukhatme (1978) had shown that the magnitude of the integral length-scale of the free-stream fluctuations has an effect on the increase of heat transfer in the stagnation region of a cylinder.

Further experiments of wake-induced unsteady heat transfer in the stagnation region of a cylinder were conducted by Magari & LaGraff (1994). Their measurements revealed the important influence of large vortical structures shed from the upstream wake-generator on heat transfer in the stagnation region. This was indirectly supported by the work of Dullenkopf & Mayle (1994) who were only moderately successful in their attempt to model the increase of heat transfer when ignoring the integral length-scale of the free-stream fluctuations. In a follow-up paper, Dullenkopf & Mayle (1995) focused on the question of how free-stream turbulence affects laminar heat transfer. For simplicity, Dullenkopf & Mayle focused on the effect of free-stream turbulence on laminar 'stagnation-like' flow having a constant acceleration. This is similar to the flow around the leading edge of a gas-turbine airfoil and the flow along the pressure side of many fore-loaded airfoils. The concepts of an 'effective' frequency (or length-scale) and an 'effective' turbulence level were developed in their study of the increase of laminar heat transfer owing to a turbulent free stream. They reported that especially free-stream fluctuations with an integral length-scale $\Lambda$ of approximately $\Lambda = 10\delta$, where $\delta$ is the boundary-layer thickness, were very effective in increasing laminar heat transfer.

The present paper reports on DNS of heat transfer and the underlying flow which were performed in a suitably chosen turbine cascade configuration with a relatively low Reynolds number. The focus of the study was on transition and laminar heat transfer effects influenced by periodically incoming wakes and the aim was to elucidate, in detail, the complex mechanisms involved. The set-up of the DNS was chosen in accordance with the experiments performed by Liu & Rodi (1994*a*, *b*), which exhibit both effects mentioned above. However, an exact copy of the experimental situation was not possible, especially with regard to the wake characteristics that must be specified as inflow conditions. Hence, the DNS and the experiments do not strictly refer to the same case and a perfect agreement should not be expected; rather, the DNS data and the chosen simulation set-up, should be regarded in their own right.

### 1.1. *Experiment simulated*

In this section, the experimental set-up on which the numerical simulations were based will be briefly discussed. For a more detailed description, see Liu & Rodi (1994*a*, *b*). The experiments were performed in a low-speed wind tunnel with a 750 mm $\times$ 750 mm cross-section. Figure 1 shows a sketch of the experimental test section. The plane wakes were generated by cylinders which were equidistantly mounted on a rotating squirrel cage, which had a diameter of 650 mm. The diameter of the cylinders was $d = 4$ mm, such that the ratio of cage diameter to cylinder diameter was 162.5 : 1. Hence, the wakes of the upward moving cylinders mounted on the upstream half of the cage would have decayed and merged producing only background turbulence by the time they reached the turbine blades. In the remainder of the paper, background fluctuations are identified with the free-stream fluctuations in between the wakes. The five turbine blades, which spanned the complete test section of 650 mm, were mounted in a linear cascade. Measurements were performed at midspan on and around the middle blade. The distance between the leading edge of the middle blade and the squirrel cage was 100 mm. The chord-length of the blades was 230 mm, while the axial chord-length was $L = 150$ mm. The pitch between blades is equal to the

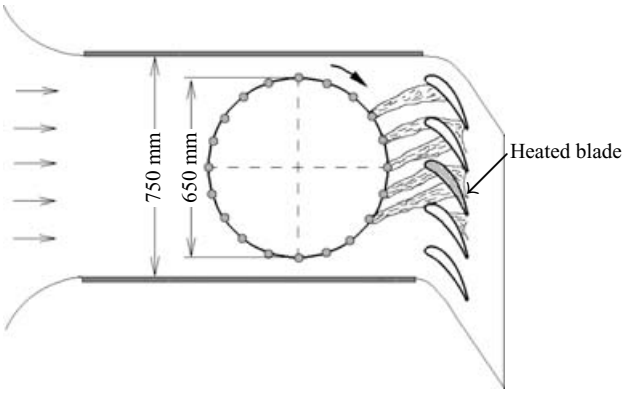


FIGURE 1. Sketch of the experimental set-up, showing a spanwise slice of the test rig.

| Case | $f$ (Hz) | $N_{cyl}$ | $D_{cyl}$ (mm) | $V_{cyl}$ | $St$ | $P$ (ms) | $Tu_{min}$ (%) |
|---|---|---|---|---|---|---|---|
| A | 0 | 0 | Inf. | 0 | 0 | Inf. | 0.9 |
| B | 60 | 24 | 85 | 5.1 | 1.84 | 16.667 | 2.3 |
| C | 120 | 24 | 85 | 10.2 | 3.68 | 8.33 | 2.8 |
| D | 180 | 48 | 42.5 | 7.66 | 5.52 | 5.56 | 3.1 |
| E | 240 | 48 | 42.5 | 10.2 | 7.36 | 4.167 | 4.8 |

TABLE 1. Overview of the experiments of Liu & Rodi (1994*a*, *b*) of which A, C and E were used as a basis for the DNS. $N_{cyl}$ gives the number of cylinders mounted on the squirrel cage, $D_{cyl}$ is the distance between two cylinders mounted on the squirrel cage, $V_{cyl}$ is the speed of the rotating cylinders, $St = fC/U$ is the Strouhal number, $C = 230$ mm is the chord length, $U = 7.5\,\mathrm{m\,s^{-1}}$ is the incoming free-stream velocity, $P = D_{cyl}/V_{cyl}$ is the period, $Tu_{min}$ is the phase-averaged background turbulence level measured at $x = 30$ mm, $L = 150$ mm is the axial chord length and the Reynolds number based on $U$ and $L$ is $Re = 72\,000$.

axial chord length $L$. The mean inflow velocity in the experiments was $U = 7.5\,\mathrm{m\,s^{-1}}$, while the speed of the moving cylinders – if present – in the cases for which DNSs were performed was $10.2\,\mathrm{m\,s^{-1}}$. The Reynolds number of the flow problem, based on $U$ and $L$ was $Re = 72\,000$. The experimental cases are given in table 1, using their original identification (see Liu & Rodi 1994*a*, *b*). Three experimental cases, A, C and E, were selected for comparison. The middle blade was kept at a uniform, slightly heated temperature and cooled by the incoming flow. The heat transfer coefficient was measured along both the suction side and the pressure side of this blade. Note that the phase-averaged turbulence level $Tu$, referred to in table 1, is defined by

$$Tu = \sqrt{\frac{1}{3}\frac{\langle u'u'\rangle + \langle v'v'\rangle + \langle w'w'\rangle}{\langle u\rangle^2 + \langle v\rangle^2}} \times 100\,\%$$

in which $\langle\cdot\rangle$ denotes phase-averaging and – because of spanwise homogeneity – $\langle w\rangle^2$ is omitted from the $Tu$ equation.

### 1.2. *Computational details*

#### 1.2.1. *Computational method*

The simulations were performed using a second-order-accurate central finite-volume discretization in space of both the incompressible three-dimensional Navier–Stokes equations and the convection–diffusion equation for the temperature, $T$, using a

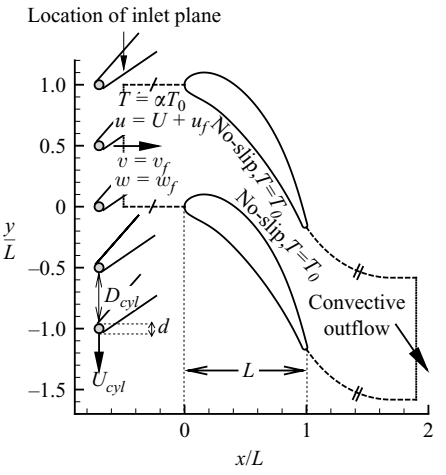


FIGURE 2. Geometry of the flow problem.

collocated variable arrangement. The Prandtl number used in the calculation of $T$ was $Pr = 0.71$. To avoid a decoupling of the velocity field and the pressure field, the momentum interpolation procedure of Rhie & Chow (1983) has been applied. The code has been parallelized using the standard MPI-protocol. To achieve a near-optimal load-balancing, the computational grid has been subdivided into blocks of equal size, each of which was assigned to its own unique processor. Time-integration has been performed using a three-stage Runge–Kutta method. More information on the basic numerical code can be found in Breuer & Rodi (1996).

1.2.2. *Computational domain and boundary conditions*

The geometry (see figure 2) and Reynolds number have been chosen in accordance with the experiments performed by Liu & Rodi (1994*a*, *b*) which are summarized above. One cascade channel is simulated. The inflow plane is located at $x/L = -0.5$ and the outflow plane is located at $x/L = 1.9$. Since the diameter of the squirrel cage is more than four times as large as the pitch between the blades, the fact that the cylinders mounted on the squirrel cage move on a circle is neglected in the simulations. Instead, the wakes are assumed to be generated by a linear row of cylinders moving in the vertical direction.

At the free boundaries of the calculation domain upstream ($x/L < 0$) and downstream ($x/L > 1$) of the blades shown in figure 2, periodic conditions were employed. For this, it is necessary that the distance between cylinders is an integer divider of the pitch between blades. On the surface of the blades, no-slip boundary conditions and a constant temperature, $T = T_0$, were prescribed. The temperature of the incoming flow was chosen to be constant, $T = \alpha T_0$, with $\alpha = 0.7$. This reflects the set-up of the experiment where the heated blade was cooled by the incoming flow. The size of the spanwise extent of the computational domain was chosen as $l_z = 0.20L$ and periodic conditions were employed at the boundaries. The choice was based on previous calculations for the T106 blade (Wissink 2003), where $0.20L$ was found to be sufficient to accommodate even the largest spanwise structures. In the outflow regions of the simulations with incoming wakes (table 2) a buffer zone was employed in which the kinematic viscosity was gradually increased from $\nu = 1/72\,000\,UL$ to $\nu = 1/5000\,UL$. In the region downstream of the buffer zone, $\nu$ was kept fixed at $1/5000\,UL$ In Simulation II the buffer zone was located between $x/L = 1.5$ and $x/L = 1.6$, whereas

| | | Wake | | $D_{cyl}$ | | $Tu_{min}$ | |
|---|---|---|---|---|---|---|---|
| Sim | Corr. Exp. | Half-width | Vel. def. | Sim. | Exp. | Sim. | Exp. |
| I | A | – | – | – | – | 0.0 % | 0.9 % |
| II | C | $0.045L$ | 30 % | $\frac{1}{2}L$ | $0.567L$ | 2.8 % | 2.8 % |
| III | E | $0.045L$ | 30 % | $\frac{1}{4}L$ | $0.284L$ | 8.4 % | 4.8 % |

TABLE 2. Overview of the direct numerical simulations performed. In all simulations a $1254 \times 582 \times 128$-point grid is employed. $Tu_{min}$ is evaluated at $x/L = -0.2$ (see also table 1) and the wake's half-width and velocity deficit are given at the inlet plane of the computational domain.

in Simulation III it corresponded to the region $1.3 \leqslant x/L \leqslant 1.5$ (see also table 2). At the outflow plane, a convective boundary condition was prescribed. As in the experiment, the pitch between blades was equal to the axial chord length $L$.

In Simulations II and III, at the inflow plane, artificial turbulent wakes $(u_w, v_w, w_w)$ and scaled background fluctuations $(u_b, v_b, w_b)$ were superposed on the mean field $(u, v, w) = U(1, 0, 0)$, giving

$$(u_{in}, v_{in}, w_{in}) = U(1, 0, 0) + (u_w, v_w, w_w) + (u_b, v_b, w_b),$$

where $(u_w, v_w, w_w) + (u_b, v_b, w_b)$ corresponds to $(u_f, v_f, w_f)$, the notation used in figure 2.

The wake data correspond to a snapshot of the instantaneous flow field of a precursor LES of a flow with similar statistical properties as found in the far field of a cylinder wake. More information on this and on the generation of the wake data and their use as inflow conditions can be found in Wu *et al.* (1999). The artificial wake data were scaled such that both the mean velocity deficit and the wake half-width agree well with the experimental data at the most upstream measurement station in front of the blade ($x/L = -0.20$, $y/L = 0.0$). Ignoring the curvature of the squirrel cage in the experiment, the artificial wakes in the numerical simulation are assumed to account for the wakes generated by a row of cylinders with $d = 0.0267L$ moving at $x/L = -0.67$ in the negative $y$-direction. It should be noted that, along the wake-axis, the distance from the cylinders to the inflow plane is about $10d$ and to the cascade entry ($x/L = 0$) $42d$, so that at these locations the wake should still have a near-field character.

The background fluctuations $(u_b, v_b, w_b)$ stem from a separate LES of 'isotropic' turbulence in a box (Dr Fröhlich, University of Karlsruhe, personal communication). The model used for the subgrid-scale stresses was the dynamic Smagorinsky model by Germano *et al.* (1991) with the modification of Lilly (1992). The resolved part of the spectrum of the fluctuations resembles the data of Comte-Bellot & Corrsin (1971). The size of the periodic box was scaled to match the spanwise size of the computational domain. By stacking five of these scaled boxes on top of one another, the entire inlet region – of size $L$ – could be covered. The fluctuations correspond to a snapshot of the turbulent field in the box and are therefore not time-dependent. To introduce time-dependency at the inflow plane, the contents of the box are swept through the inlet along the $x$-axis. Each time step $\delta t$, the box is moved by a distance of $U\delta t$. When the end of the periodic box has been reached, the box is moved back to its original location and the operation starts again. The integral length scale $\Lambda$ associated with the background fluctuations from the scaled box is $\Lambda \approx 0.019L$.

The Taylor micro-scale $\lambda$ of these fluctuations is $\lambda \approx 0.008L$. For the artificial wakes, the integral length scale in the spanwise direction, $\Lambda \approx 0.027L$, was found to be an order of magnitude larger than the integral length scale in the direction normal to the symmetry plane of the wake, which is still much smaller than the width of the wake at the inflow of about $0.1L$. The artificial wakes mimic the far-field behaviour of a turbulent wake with relatively small scales, while in the experiment the wakes probably still contained larger-scale coherent structures of size comparable to the wake width when entering the domain covered by the computation and also the passage between blades.

The three simulations that were performed are itemized in table 2. In Simulation I, no wakes were introduced at the inflow plane. In Simulation II, the period of the wakes was $P = \frac{1}{2}L/(1.36U) = 0.3676L/U$, while in Simulation III this period was $P = \frac{1}{4}L/(1.36U) = 0.1838L/U$. In order to allow the use of periodic boundary conditions in the vertical direction, compared to Experiments C and E given in table 1, the actual distance between two cylinders has been slightly modified such that the ratio of the blade pitch ($=L$) and $D_{cyl}$ becomes an integer number (see also table 2, where the actual distance between two adjacent cylinders in terms of axial chord length is given). Also note the differences between Experiments A and E and Simulations I and III, respectively, regarding the minimum turbulence levels in the first measurement plane, $x/L = -0.20$. Only for Simulation II was a series of preliminary LES-runs performed in order to determine the level of the background fluctuations to be added at the inflow plane in order to reach the same minimum $Tu$-level in the plane $x/L = -0.20$ as in Experiment C. The $Tu$-level employed at the inlet of Simulation III was then extrapolated from the $Tu$-level used in Simulation II. Because in this case the wakes introduced at the inlet of the simulation unexpectedly merged upstream of $x/L = -0.20$, a further increase in $Tu$ to the high values shown in table 2 resulted. Unfortunately, it was too expensive and too time-consuming to perform further runs. To illustrate that the fluctuations, the mean wake deficit and the wake half-width, introduced at the inflow plane in Simulation II, give a reasonable representation of the experimental values (Case C), a comparison is made of phase-averaged velocity and r.m.s. quantities as a function of phase $\phi$ at $(x/L, y/L) = (-0.20, 0.0)$. All data were normalized by the mean inflow velocity $U$, while the time-coordinate in the experimental data was also scaled by a factor of 0.5/0.567 to account for the difference in cylinder distance, $D_{cyl}$, between Simulation II and the experiment C mentioned above (see also tables 1, 2). As shown in figure 3($a$), for Simulation II the phase-averaged blade-parallel velocity, $\langle u \rangle$, and its r.m.s.-value agree well with experiment. On the other hand, the experimental level of the phase-averaged blade-normal velocity, $\langle v \rangle$, shown in figure 3($b$) together with its r.m.s.-value is found to be consistently about $0.1U$ lower than in Simulation II. This difference is due to a slight difference in inflow angle between the experiment and the DNS. However, the agreement of the mean wake velocity deficit and the half-width of the wake is quite good. Finally, the phase-averaged r.m.s. value of the $v$-velocity of Simulation II is also in good agreement with Experiment C. In Simulation III, both the mean wake velocity deficit and the wake half-width are in agreement with experiment, while – as mentioned earlier – the level of the background fluctuations is too large.

### 1.2.3. *Computational mesh*

The mesh at midspan is illustrated in figure 4. It was generated using the elliptic mesh generator of Hsu & Lee (1991) and it was optimized using experience gained in

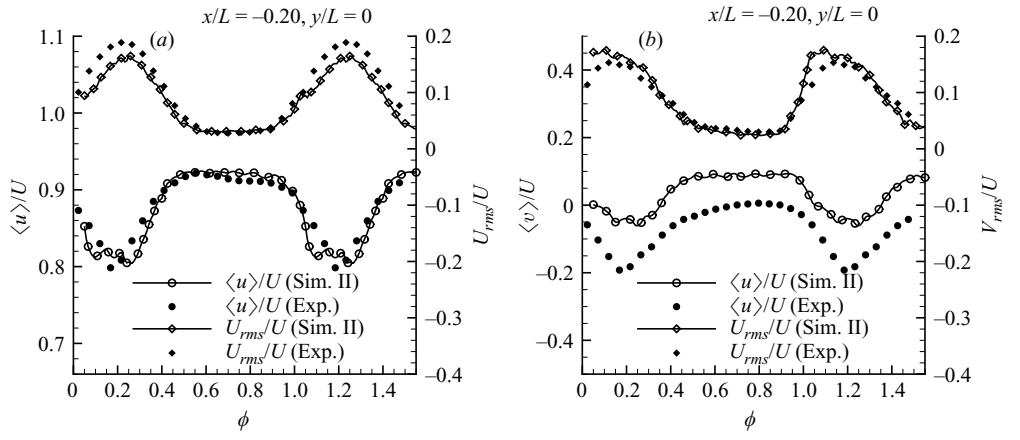


FIGURE 3. Comparison of phase-averaged velocity and r.m.s. profiles at $x/L = -0.20$, $y/L = 0.0$, (*a*) *u*-velocity; (*b*) *v*-velocity, as a function of phase $\phi$, Simulation II *vs.* Experimental case C.

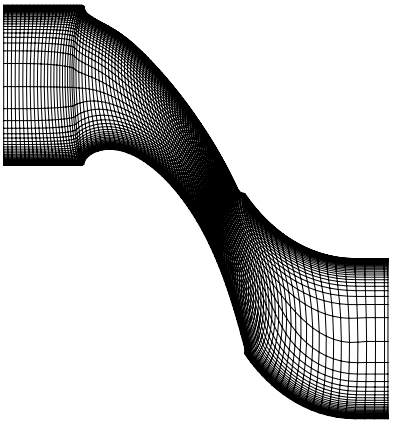

FIGURE 4. Computational mesh showing every twelfth gridline in the $(x,y)$-plane.

earlier DNS and LES of periodic unsteady flow in a T106 cascade, see also Michelassi *et al.* (2002) and Wissink (2003). The mesh provides an adequate resolution of both the suction-side and the pressure-side boundary-layers. The calculations were performed on the Hitachi SR8000-F1 of the Leibniz Computing Centre in Munich using 93.4 Mio. grid points and 256 processors. The time step employed in the simulations was $\delta t \approx 3 \times 10^{-5} L/U$. To complete the simulations, for Simulation I, 150 000 time steps were required, whereas for Simulations II and III, 240 000 time steps were required. As a result, for Simulation I, approximately one and a half months (1250 clock hours) of continuous running was required, whereas for each of the Simulations II and III almost three months (2000 clock hours) of runtime was required. Figure 5 shows the grid-resolution along the suction side of the blade. It illustrates that the boundary layer is reasonably resolved. The distance between the wall and the wall-nearest grid-point in wall units, $\Delta y^+$, mostly fluctuated around 1.5, indicating that the viscous sublayer was reasonably well resolved. $\Delta x^+$ was mostly between 20 and 30 wall units, while $\Delta z^+$ assumed values around 15 wall units, respectively. The number of computational points in the wall-normal direction inside the suction-side boundary-layer increased

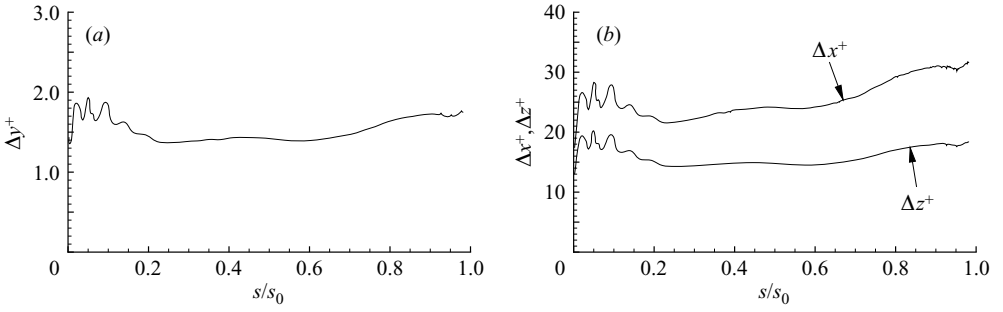


FIGURE 5. Distances between points in wall-units along the suction side for Simulation II. (*a*) wall-adjacent point to the surface. (*b*) Wall-parallel point-to-point

from 12 near the leading edge, at $s/s_0 = 0.05$, to more than 90 near the trailing edge. Along the pressure side, moving from the leading edge towards the trailing edge, $\Delta y^+$ increased from less than 1 to 1.5, $\Delta x^+$ increased approximately from less than 12 to 25 and $\Delta z^+$ increased from less than 10 to 15. The number of grid points in the wall normal direction inside the pressure-side boundary-layer increased from 15 near the leading edge to approximately 40 near the trailing edge. To check whether the wall-normal grid-size, $\Delta y$, near the suction side would be sufficiently small to resolve isotropic turbulence (which we do not have), the ratio $\Delta y/\eta$, where $\eta$ is the Kolmogorov length scale, was determined. For isotropic turbulence, the Kolmogorov length scale is defined by $\eta = (\nu^3/\varepsilon)^{1/4}$, where $\nu = 1/72000UL$ is the kinematic viscosity and $\epsilon$ is the rate of dissipation of the time-averaged kinetic energy of the fluctuations, $\bar{k} = \frac{1}{2}\overline{u_i' u_i'}$, and is defined by

$$\varepsilon = \nu \left( \overline{\frac{\partial u_i'}{\partial x_j} \frac{\partial u_i'}{\partial x_j}} \right).$$

To determine $\varepsilon$, 240 snapshots of the fluctuating velocity $\boldsymbol{u}' = (u', v', w')$ – covering two periods $P$ – were employed. According to Pope (2000), to resolve the mode at which dissipation is maximum, we must be able to resolve a length scale of approximately $24\eta$. Up to a distance of $2\delta$ from the wall, where $\delta$ is the boundary-layer thickness, the ratio $\Delta y/\eta$ was always found to be smaller than 4, which means that there were at least 6 grid points available to resolve the mode with maximum dissipation. Farther away from the surface, $\Delta y/\eta$ slowly increased and assumed values up to 9.5 in the region with a maximum distance of $4\delta$ from the wall, which corresponded to about 3 grid points per wave mode. Note that because of the severe straining by the external flow, the free-stream fluctuations within the passage between blades will not be isotropic. Hence, the above results are no more than an indication that the computational mesh in the near-wall region was sufficiently fine to resolve the important length scales of the turbulent flow.

### 1.2.4. *Phase-averaged statistics*

The velocity field $\boldsymbol{u}$ can be written as $\boldsymbol{u} = \overline{\boldsymbol{u}} + \tilde{\boldsymbol{u}} + \boldsymbol{u}'$, where $\overline{\boldsymbol{u}}$ is the time-averaged velocity field, $\tilde{\boldsymbol{u}}$ represents velocity fluctuations with period $P$, and $\boldsymbol{u}'$ are the remaining velocity fluctuations. The phase-averaged velocity field $\langle \boldsymbol{u} \rangle$ is the sum of the time-averaged velocity field and the velocity fluctuations with period $P$, i.e. $\langle \boldsymbol{u} \rangle = \overline{\boldsymbol{u}} + \tilde{\boldsymbol{u}}$. In Simulation II, the flow was allowed to develop for 10 periods, followed by a subsequent phase-averaging over 10 further periods. In Simulation III, 20 periods

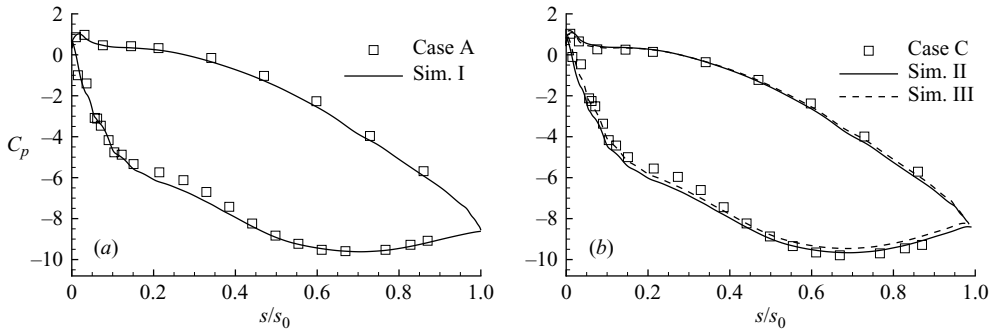


FIGURE 6. Wall static-pressure coefficient $C_p$ along the turbine blade for (*a*) Simulation I and (*b*) Simulations II and III and comparison to experiment.

were required to obtain a well-developed flow field, while phase-averaged statistics were gathered during 20 subsequent periods. In the phase-averaging procedure, each period was subdivided into 120 equal phases, $\phi = 0, 1/120, \ldots, 119/120$. For each of the phases, 15 spanwise-averaged $(x, y)$-fields containing phase-averaged statistics were stored.

Note that in the remainder of the paper 'kinetic energy of the fluctuations' or – more briefly – 'kinetic energy' always refers to 'phase-averaged kinetic energy of the fluctuations $\langle k \rangle$', unless it is explicitly specified that it is the time-averaged variant $\overline{k}$.

## 2. Results

### 2.1. *General flow characteristics*

#### 2.1.1. *Time-averaged statistics of the flow field*

The wall static-pressure coefficient $C_p$ is defined by

$$C_p = \frac{\overline{P} - \overline{P}_{ref}}{\frac{1}{2}U_{ref}^2},$$

where $\overline{P}$ is the mean pressure, $\overline{P}_{ref}$ is the time-averaged pressure at $P_1$ : $(x/L, y/L) = (-0.20, 0.50)$ – located in the centre of the inflow region upstream of the blades – and $U_{ref}$ is the magnitude of the time-averaged velocity at $P_1$. In figure 6, $C_p$ is plotted for Simulation I (figure 6*a*) and Simulations II and III (figure 6*b*), in comparison with Experiments A and C, respectively, and the agreement can be seen to be good. The small difference between Case A and Case C of the experiments indicates that the incoming wakes and the free-stream turbulence only have a moderate effect on the mean $C_p$ distribution. This is also evidenced by the fact that the increase in the level of incoming disturbances in Simulation III, compared to Simulation II, is found not to affect the $C_p$ distribution. The agreement between Experiment A and the Simulation I indicates that the effect of the background fluctuations in the experiment on the $C_p$ distribution is negligible. Figures 6(*a*) and 6(*b*) show that in all simulations, the streamwise pressure gradient along the pressure side is mostly strongly favourable, except for a small region around $s/s_0 = 0.15$ where it is only slightly favourable. Hence, the flow along the entire pressure side is accelerating. Along the suction side, the streamwise pressure gradient is favourable for $s/s_0 < 0.65$. Further downstream, the pressure gradient becomes adverse. As a consequence, the

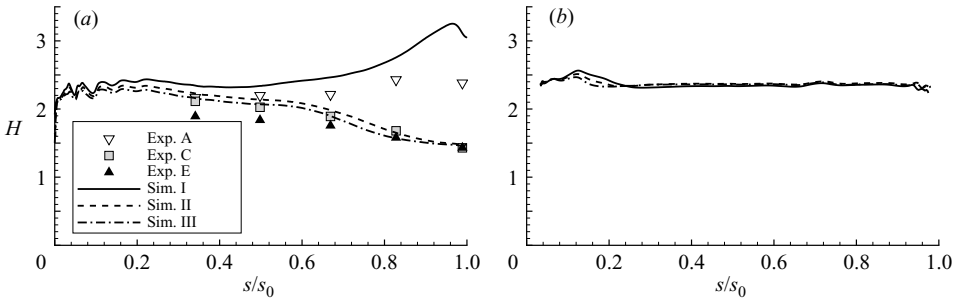


FIGURE 7. Comparison of the time-averaged shape factor, $H$, as a function of the normalized wall-coordinate ($a$) suction side, ($b$) pressure side. Simulations I, II, III and Experiments C, E (only along suction side).

boundary-layer flow in this region is less stable and, in the presence of incoming disturbances, transition is likely to occur.

Figure 7($a$) shows a comparison of the time-averaged shape factors, $H$ (for a definition see Pope 2000), along the suction side between Simulations I, II, III and Experiments A, C, E, respectively. In Simulation I – without wakes – the boundary layer remains laminar and goes towards separation in the APG region resulting in an increase in $H$. Compared to Experiment A, $H$ is found to be in reasonably good agreement upstream of $s/s_0 \approx 0.65$, while farther downstream the background fluctuations in Experiment A cause the boundary-layer flow to become mildly transitional, thereby inhibiting the growth of $H$.

Simulations II and III – with wakes – are in reasonably good agreement with experiments C and E, respectively. Compared to the experiments, in the region between $s/s_0 = 0.20$ and $s/s_0 = 0.85$, $H$ is only slightly larger in the numerical simulations. The increased wake frequency and level of background fluctuations in Simulation III and Experiment E causes a stronger triggering of the boundary-layer flow resulting in a slight decrease in $H$ as compared to Simulation II and Experiment C, respectively. As the streamwise pressure gradient turns adverse, the suction-side boundary-layer flow undergoes transition reflected by a continuous decrease of the shape factor towards the trailing edge in both Simulations II and III. Immediately upstream of the trailing edge, the boundary-layer flow has turned mildly turbulent, which is reflected in $H$ assuming values around $H = 1.5$.

Figure 7($b$) shows a comparison of the time-averaged shape factors along the pressure side obtained in the Simulations I–III. The shape factors obtained in the three simulations are nearly the same and assume values which indicate that the pressure-side boundary-layer remains completely laminar.

Profiles of the r.m.s. values of the streamwise velocity fluctuations near the suction side are shown in figure 8. The large difference between Experiment A and Simulation I, observed in figure 8($a$), is due to the free-stream fluctuations which are present only in the experiment. These background fluctuations trigger fluctuations inside the boundary layer so that their level increases in the streamwise direction. Because of the absence of free-stream fluctuations in Simulation I, the entire suction-side boundary-layer remains virtually laminar. Figure 8($b$) shows a relatively good agreement between the fluctuations in Simulation II and Experiment C. Only at $s/s_0 = 0.989$ are the free-stream fluctuations larger than in the experiment. The good agreement of r.m.s. values in the boundary layer is a direct result of the good match of the wake velocity-deficit and the fluctuations in the plane $x/L = -0.20$, illustrated in figure 3. The overestimation of the fluctuations at this plane in Simulation III is a consequence of

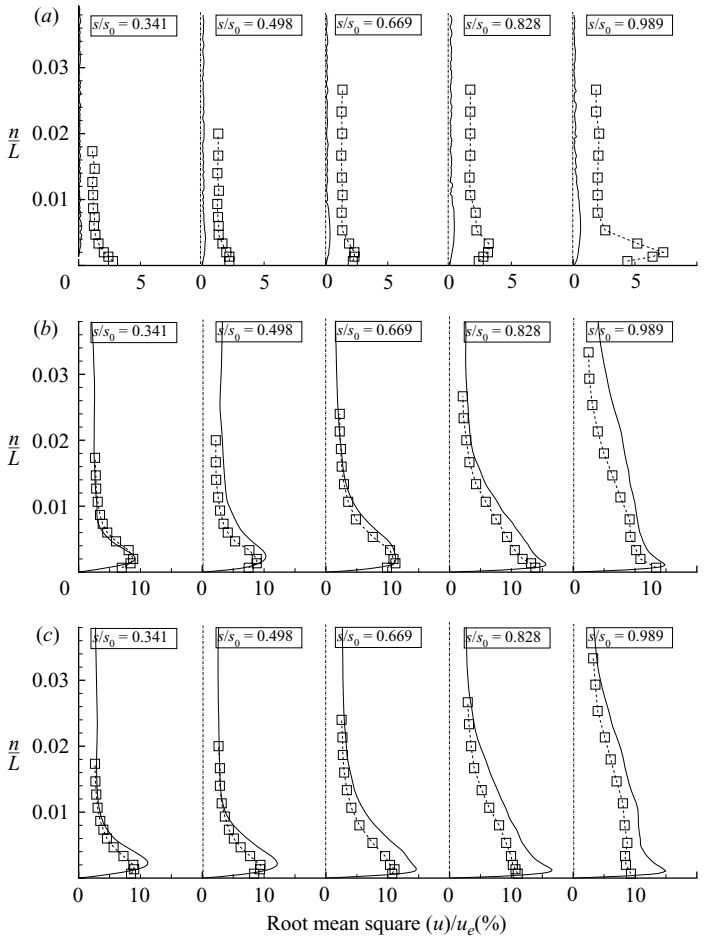


FIGURE 8. Profiles of the r.m.s. values of blade-parallel velocity fluctuations along the suction side for (*a*) Simulation I *vs.* Experiment A; (*b*) Simulation II vs. Experiment C; (*c*) Simulation III *vs.* Experiment E. □, experiments; ——, DNS.

the excessive free-stream disturbances added at the inflow (see tables 1 and 2) which lead to a stronger triggering of unstable modes in the boundary-layer flow. As a result, at $s/s_0 = 0.828$ and 0.989 the maximum level of fluctuations is overestimated by more than 30 %.

Figure 9 shows the time-averaged skin-friction coefficient, $C_f$, along the suction side (figure 9*a*) and the pressure side (figure 9*b*) of the blade. Along the suction side, the $C_f$-values obtained in Simulations I, II and III are found to be nearly identical in the region $0.10 < s/s_0 < 0.5$. Near the leading edge, the disturbances impinging in Simulations II and III manage to introduce instabilities into the boundary-layer flow which result in slightly elevated skin-friction levels. These instabilities are subsequently damped in the downstream direction owing to the FPG in the region $s/s_0 < 0.65$ (see figure 6). For $s/s_0 > 0.65$, the pressure gradient turns adverse and, consequently, the boundary-layer flow becomes more susceptible to impinging disturbances – which eventually lead to boundary-layer transition. Hence, there is a progressively increasing difference in $C_f$ between Simulation I and Simulations II and III. Compared to Simulation II, in Simulation III both the background disturbances and the frequency

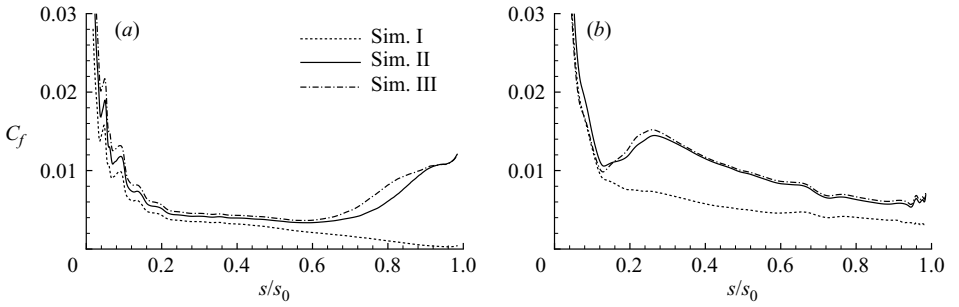


FIGURE 9. Comparison of the time-averaged skin-friction coefficient, $C_f$, as a function of the normalized wall coordinate; Simulations I, II and III. (*a*) Suction side, (*b*) pressure side.

of the impinging wakes are increased. As a consequence, transition occurs slightly earlier and the increase in $C_f$ is shifted slightly upstream.

Along the entire pressure side, upstream of $s/s_0 = 0.10$, the skin friction coefficients in all simulations more or less coincide. For larger $s/s_0$, the skin friction in Simulations II and III then grows in the downstream direction until it reaches a peak at $s/s_0 = 0.28$. Downstream of this location, the $C_f$ level continuously decreases again. The elevated level of $C_f$ observed in Simulations II and III (as compared to Simulation I) is a direct consequence of the longitudinal vortical structures introduced into the pressure-side boundary-layer by the impinging wakes (see figure 19). Whereas for $s/s_0 < 0.28$ the pressure-side streamwise pressure-gradient is only mildly favourable, for larger $s/s_0$ it becomes increasingly negative and thereby progressively damps boundary-layer disturbances (see also figure 6). Despite the drastic increase in the level of the free-stream fluctuations in Simulation III, compared to Simulation II, the $C_f$ level is only slightly elevated for $s/s_0 > 0.12$.

### 2.1.2. *Phase-averaged statistics of the flow field*

Figure 10 shows the influence of the impinging wake on the phase-averaged shape factor at eight different phases, $\phi = 0, 1/8, \ldots, 7/8$, along the suction side of the blade in Simulation II. The graph at the bottom shows the time-averaged shape factor and the envelope of the phase-averaged signals $\langle H \rangle$. This envelope illustrates the extreme values of the phase-averaged signals. The approximate location of the impinging wakes is labelled 'W'. Disturbances introduced by impinging wakes into the boundary layer can be seen to decrease locally the phase-averaged shape factor. At $\phi = 3/8$, the wake-induced local magnitude of $\langle H \rangle$ reaches a value of 1.8 at $s/s_0 \approx 0.72$. This local minimum indicates the presence of a wake-induced turbulent patch inside the suction-side boundary-layer. For $\phi = 4/8, 5/8$, the wake-affected $\langle H \rangle$ reaches values around and below 1.6. Near the trailing edge, the suction side boundary-layer flow appears to remain mildly turbulent for all phases as the shape factor assumes values around 1.5. The envelope of $\langle H \rangle$ shown in the lower graph illustrates that the temporal variation in $\langle H \rangle$ gradually grows along the suction side until it reaches a peak near $s/s_0 \approx 0.82$. Apparently, in this region, the flow is highly intermittent. This intermittency is related to the periodically impinging wakes which introduce disturbances into the boundary-layer flow that are subsequently convected downstream into the mildly turbulent region.

Figure 11 shows the time-averaged shape factor and the envelope of the phase-averaged signals $\langle H \rangle$ obtained along the pressure side of the blade in Simulation II. The time-averaged shape factor is almost constant and the influence of the impinging

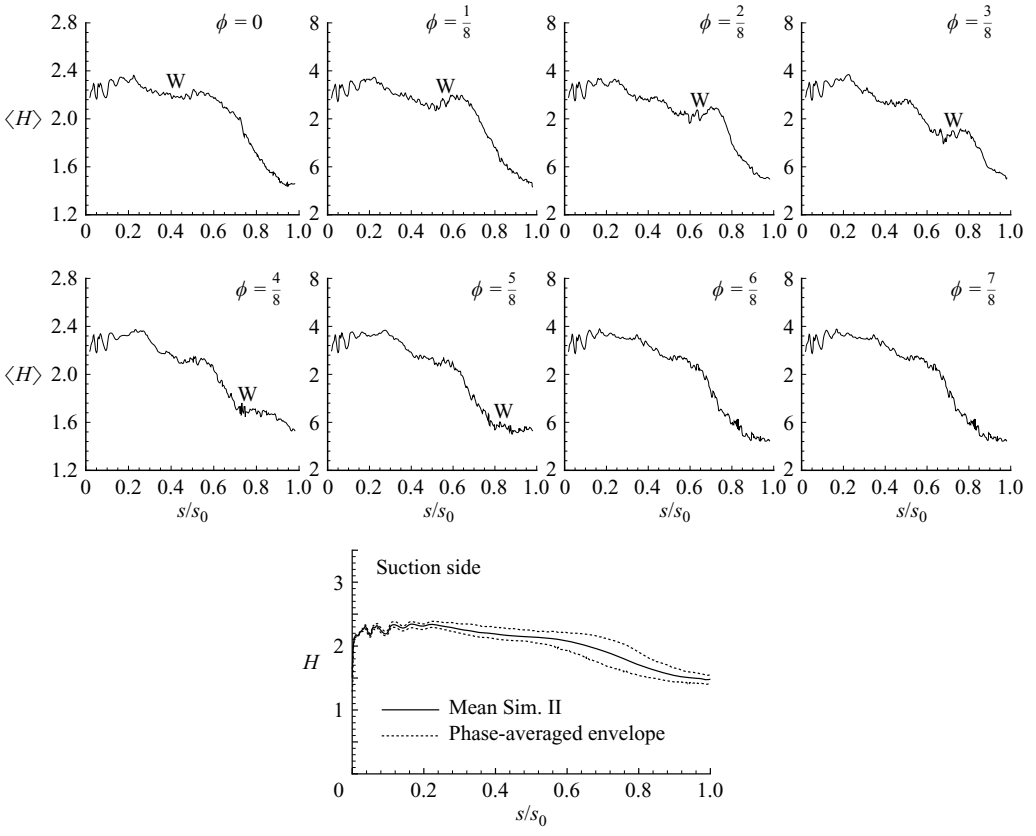


FIGURE 10. Simulation II: the upper graphs show the phase-averaged shape factor, $\langle H \rangle$, along the suction side as a function of the normalized surface coordinate $s/s_0$. The approximate location of the impinging wake is identified by the label 'W'. The graph at the bottom shows the time-averaged shape factor together with the envelope of the phase-averaged shape factor.

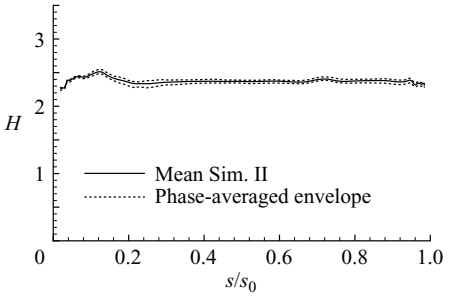


FIGURE 11. Simulation II: time-averaged shape factor along the pressure side together with the envelope of the phase-averaged shape factor.

wakes on the shape factor along the pressure side of the blade can be seen to be small.

Figure 12 shows profiles of the phase-averaged turbulent shear stress, $\langle u'v' \rangle$, kinetic energy of the fluctuations, $\langle k \rangle$, and spanwise turbulent stress, $\langle w'w' \rangle$, for three phases $\phi = 0, 3/8, 6/8$, at two locations $s/s_0 = 0.60$ and $s/s_0 = 0.90$ on the suction side from Simulation II. At $s/s_0 = 0.60$, the $\langle u'v' \rangle$ profiles clearly show the influence of the

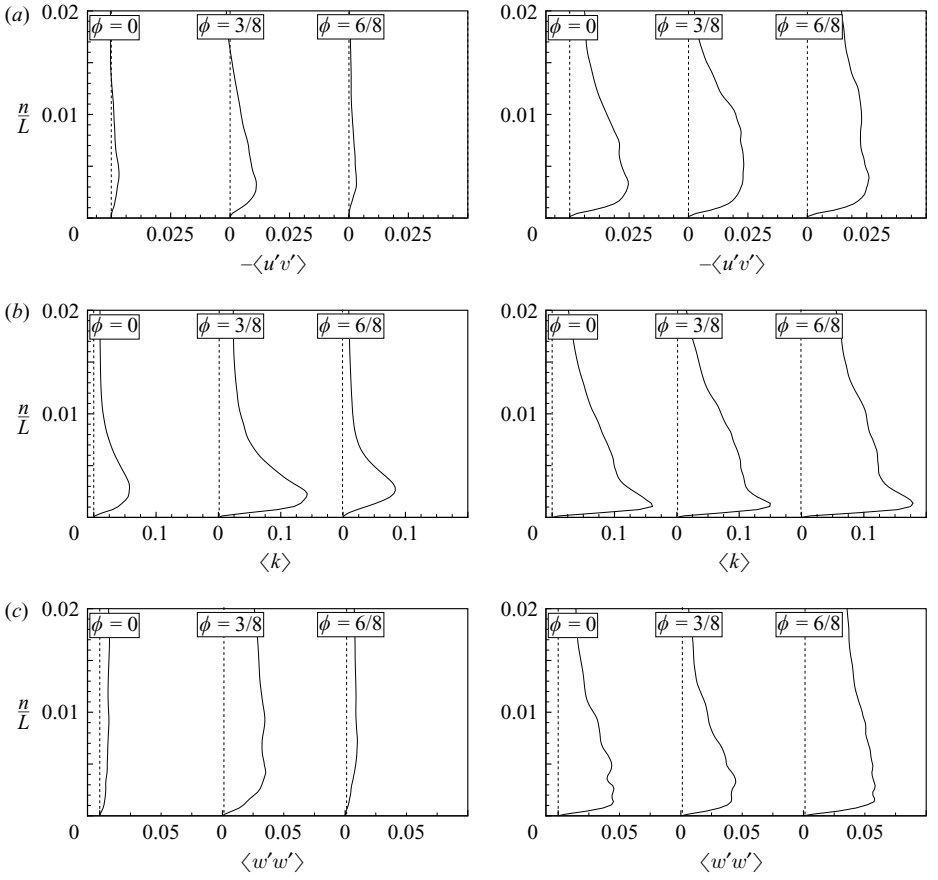


FIGURE 12. Simulation II: suction side: normal profiles at $s/s_0 = 0.60$ (left) and $s/s_0 = 0.90$ (right) of the phase-averaged shear stress, $\langle u'v' \rangle$ – where $u'$ are the fluctuations in the blade-tangential direction and $v'$ are the fluctuations in the blade-normal direction –, kinetic energy, $\langle k \rangle$, and spanwise turbulent stress $\langle w'w' \rangle$, all made dimensionless using $U^2$. The profiles correspond to three phases $\phi = 0, 3/8, 6/8$.

impinging wake at $\phi = 3/8$, giving rise to an increase of $-\langle u'v' \rangle$. At $s/s_0 = 0.90$, the $\langle u'v' \rangle$-profiles are very similar for all phases indicating that the influence of the impinging wakes has diminished. This confirms further that at $s/s_0 = 0.90$, the boundary layer is less sensitive to impinging disturbances from the outside as it has turned mildly turbulent as indicated already by the behaviour of the shape factor.

The influence of the impinging wakes on the phase-averaged kinetic energy of the fluctuations inside the suction-side boundary-layer is found to be significant. All profiles show a maximum in $\langle k \rangle$ located inside the suction-side boundary-layer. Compared to $s/s_0 = 0.60$, at $s/s_0 = 0.90$, for all phases the locations of the maximum $\langle k \rangle$ are much closer to the surface, which is related to the fact that the boundary layer at this location is already mildly turbulent.

Figure 12(*c*) shows that at $s/s_0 = 0.60$, relatively large spanwise fluctuations $\langle w'w' \rangle$ are intermittently present in the free stream (for instance at $\phi = 3/8$). In the suction-side boundary-layer itself, only low-level spanwise fluctuations were observed. At $s/s_0 = 0.90$, spanwise fluctuations are permanently stronger and located inside the suction-side boundary layer, which is to be expected for a turbulent boundary layer.

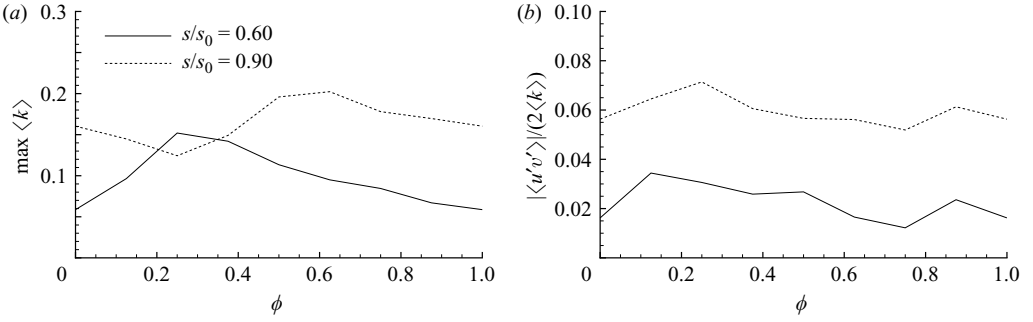


FIGURE 13. Suction side of Simulation II: (*a*) maximum of $\langle k \rangle$ at $s/s_0 = 0.60$ and $s/s_0 = 0.90$ as a function of phase, (*b*) Townsend's structural parameter $|\langle u'v' \rangle|/2\langle k \rangle$ at $s/s_0 = 0.60$ and $s/s_0 = 0.90$ as a function of phase, where $\phi = 0, 1/8, \ldots, 7/8, 1$, at $\Delta y^+ \approx 16$.

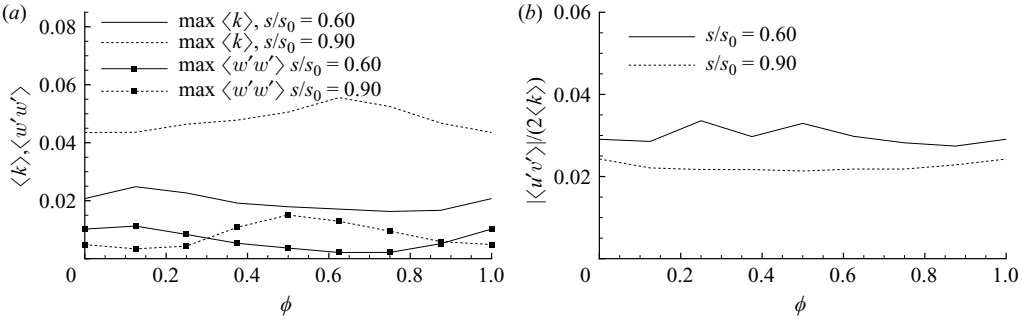


FIGURE 14. Pressure side of Simulation II: (*a*) maxima of $\langle k \rangle$ and $\langle w'w' \rangle$ at $s/s_0 = 0.60$ and $s/s_0 = 0.90$ as a function of phase, (*b*) $|\langle u'v' \rangle|/2\langle k \rangle$ at $s/s_0 = 0.60$ and $s/s_0 = 0.90$ as a function of phase. Both quantities have been made dimensionless using $U^2$.

In figure 13(*b*), the structure parameter $|\langle u'v' \rangle|/2\langle k \rangle$ on the suction side in Simulation II is plotted as a function of phase at both $s/s_0 = 0.60$ and 0.90 and a wall-distance of $y^+ \approx 16$. The instant of impingement of the wake is easily identified in figure 13(*a*) by the instant at which $\langle k \rangle$ has a peak. At $s/s_0 = 0.60$, the structure parameter varies around 0.025, whereas at $s/s_0 = 0.90$ it varies around 0.06. Both values are much smaller than the value of 0.15 which is typical for a fully turbulent boundary layer in the presence of a small or zero pressure gradient. This gives evidence that the boundary layer at $s/s_0 = 0.60$ is mostly laminar, with some superimposed fluctuations induced by the wakes and background fluctuations, and at $s/s_0 = 0.90$ it is only intermittently turbulent. In the vicinity of this location, evidence of by-pass transition with turbulent spots that grow and merge in the downstream direction was found.

Compared to the suction side, on the pressure side at both locations the shear stress is found to be an order of magnitude smaller. The influence of individual impinging wakes – causing a phase-dependency in the phase-averaged signals $\langle u'v' \rangle$, $\langle k \rangle$ and $\langle w'w' \rangle$ on the suction side (see figure 12) – is found to be significantly reduced for both $\langle u'v' \rangle$ and $\langle k \rangle$. Only the spanwise stresses show a non-negligible influence of impinging wakes along the pressure side, as evidenced in figure 14(*a*) which shows the maxima of $\langle k \rangle$ and $\langle w'w' \rangle$ as a function of phase. Compared to the $\langle k \rangle$ values, however, these spanwise stresses are relatively insignificant. The very small $\langle u'v' \rangle$

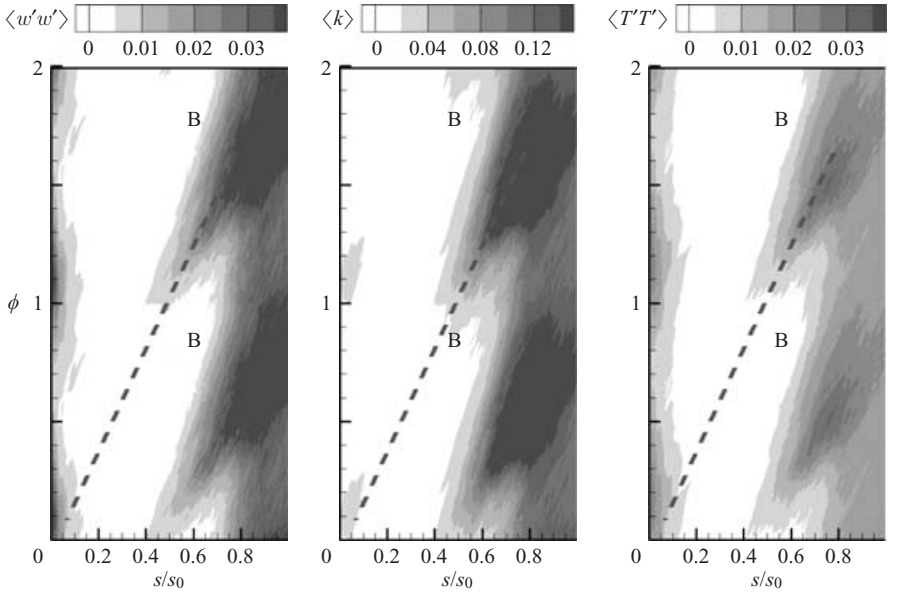


FIGURE 15. Simulation II: space–time plots showing contours of the phase-averaged spanwise stress, $\langle w'w' \rangle$, kinetic energy of the fluctuations, $\langle k \rangle$, and temperature variance, $\langle T'T' \rangle$, along a grid-line at a distance of approximately $0.000752L$ from the suction side of the blade. $\langle w'w' \rangle$ and $\langle k \rangle$ have been made dimensionless using $U^2$, while $\langle T'T' \rangle$ has been made dimensionless using $T_0^2$.

values indicate once more that the pressure-side boundary-layer is laminar at both locations, while the non-negligible $\langle k \rangle$ values give evidence of large-scale fluctuations along the pressure side. Though the spanwise component of these fluctuations is not very large, compared to the shear stress it is certainly non-negligible. The largest component contributing to $\langle k \rangle$ is by far the normal stress $\langle u'u' \rangle$ in the streamwise direction. This large contribution is due to the longitudinal vortical structures present along the pressure side (see figure 19), which were also observed by Wu & Durbin (2001) and Wissink (2003). These structures promote the vertical exchange of fluid. Low-speed fluid from the inner part of the boundary layer is moved towards the outer part, while high-speed fluid is moved from the outer part towards the inner part, resulting in the observed large fluctuation in the near-wall streamwise velocity.

Figure 14(*b*) shows the structure parameter for $s/s_0 = 0.60$ and $s/s_0 = 0.90$ at a distance of approximately $y^+ = 16$ wall-units on the pressure side in Simulation II. Again, the local peaks observed in the 'maximum $\langle k \rangle$' signals are caused by the impingement of wakes. As expected, the comparatively low values of the phase-averaged shear stress induce very small values of $|\langle u'v' \rangle|/2\langle k \rangle$ at both locations. This provides further evidence that the pressure-side boundary-layer remains laminar for all phases. The large values of $\langle k \rangle$, explained above, obviously contribute to the low values obtained for the structure parameter.

Figure 15 shows space–time contour plots of the phase-averaged spanwise stress, $\langle w'w' \rangle$, the kinetic energy of the fluctuations, $\langle k \rangle$, and the temperature variance $\langle T'T' \rangle$ along a grid line at a distance of $0.0752\,\%L$ from the suction side of the blade as obtained in Simulation II – corresponding to $y^+$ values varying between 6 and 9. For reference purposes, the approximate path of the wake is identified by a

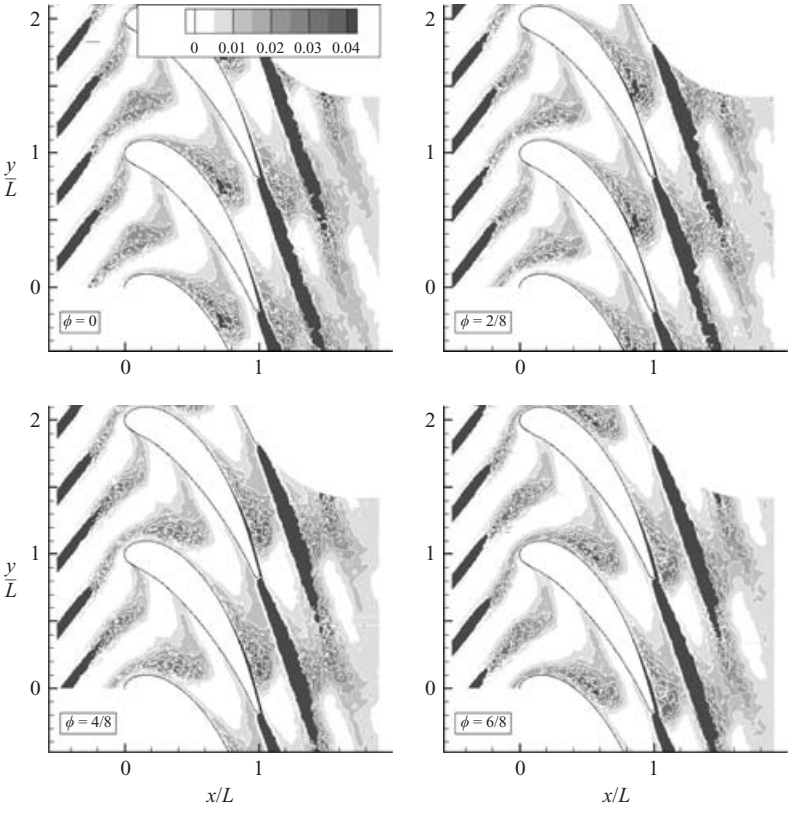


FIGURE 16. Simulation II: development of the phase-averaged kinetic energy, $\langle k \rangle$, in the vane of the turbine cascade. $\langle k \rangle$ has been made dimensionless using $U^2$.

dashed line. All contour plots clearly illustrate that the periodically impinging wakes trigger disturbances in the boundary layer. During the phases at which the wakes do not impinge, these disturbances are convected downstream. As a result, so-called 'becalmed regions' (labelled 'B' in figure 15) appear. At the leading edge, contours of spanwise fluctuations stemming from periodic impinging wakes are clearly visible in the $\langle w'w' \rangle$-graph and – because of the applied scaling – only marginally in the $\langle k \rangle$-graph. The contour plot of the temperature variation shows that the impinging wakes introduce temperature fluctuations close to the surface of the blade. This effect is clearly visible both near the leading edge and along the downstream half of the suction side of the blade. In the latter region, a local maximum of $\langle T'T' \rangle$ at $(s/s_0, \phi) \approx (0.8, 0.5)$ is observed.

In figure 16, contours of the phase-averaged kinetic energy of the fluctuations, $\langle k \rangle$, are shown at mid-span in Simulation II at four phases $\phi = 0, 2/8, 4/8, 6/8$. The sequence of graphs clearly illustrates the initial decay of disturbances carried by the wakes in the inlet region and the deformation of the wake as it travels through the passage between the blades. As observed earlier for the T106 turbine blade (Wu & Durbin 2001; Wissink 2003), the wake more or less wraps around the leading edge, is stretched by the accelerating flow and subsequently impinges on the suction side at virtually zero angle of attack. Along the pressure side, the angle between the wake and the surface of the blade is approximately 45° immediately downstream of the leading edge and subsequently gradually decreases until it reaches a value of approximately

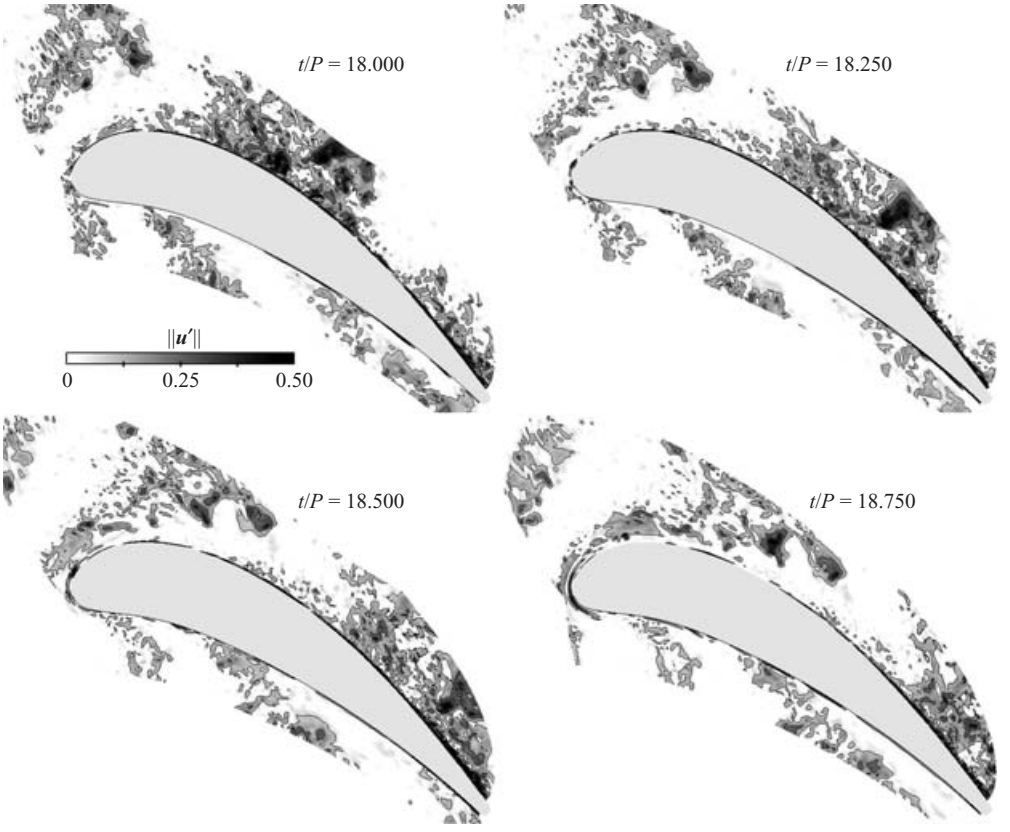


FIGURE 17. Simulation II: snapshots of the magnitude of the fluctuating velocity – made dimensionless using $U$ – at mid span.

0° at the trailing edge. Inside the passage between blades, at the apex of the deformed wake, significant production of kinetic energy can be observed. The contours of $\langle k \rangle$ are somewhat irregular because of the limited number of 10 phases employed in the phase-averaging procedure. As already illustrated in figure 12, along the downstream half of the suction side, the wakes trigger non-negligible amounts of kinetic energy in the boundary layer. This is reflected by the presence of dark contours in the APG-region of the suction side surface which thicken towards the trailing edge. The kinetic energy level of the background fluctuations is less than 0.005 and is therefore not visible in the contour plots, which allows the location of the wakes to be easily identified by the higher concentrations of kinetic energy.

2.1.3. *Instantaneous flow patterns*

Figure 17 shows snapshots of the fluctuating velocity field $||\boldsymbol{u}'|| = ||\boldsymbol{u} - \langle \boldsymbol{u} \rangle||$ at mid-span obtained in Simulation II at four instants in order to visualize some of the dynamics of the flow during one period $P$. The snapshots illustrate the presence of fluctuations inside the periodically oncoming wakes and the amalgamation of disturbances at the apex of the wake, somewhat above the suction side surface. Comparing the snapshot taken at $t/P = 18.25$ with the one at $t/P = 18.50$ shows the increase in boundary-layer disturbances immediately upstream of the trailing edge owing to the impinging wake. Because of the strong favourable streamwise pressure gradient in the leading-edge region $s/s_0 < 0.1$ (see figure 6), stretching is very strong

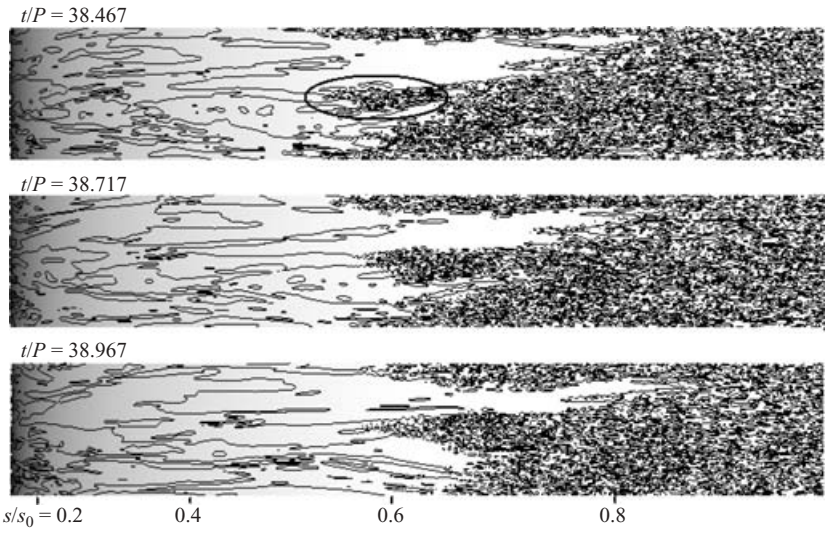


FIGURE 18. Simulation III: sequence of snapshots of contours of the instantaneous velocity in the $y$-direction in a plane at a distance of $0.0018L$ from the suction side of the blade, showing evidence of a turbulent spot, identified by the black ellipse, in the adverse-pressure-gradient region of the suction-side boundary-layer.

and the fluctuations carried in this part of the wake are significantly damped. The latter is visible in the snapshots taken at $t/P = 18.00$ and $t/P = 18.25$. Generally, in the FPG region along the suction side, vortex-stretching results in the emergence of thin longitudinal vortical structures which impinge on the boundary layer at virtually zero angle of attack (see Wissink 2003). Figure 6 also shows that along the pressure side, the streamwise pressure gradient becomes increasingly favourable downstream of $s/s_0 = 0.15$. In a thin layer adjacent to the pressure side, slight fluctuations in the velocity field can be observed for all phases. These fluctuations do not only occur at the locations where the wakes impinge, but are also found in regions where no wakes are impinging. The latter is directly related to the presence of longitudinal vortical structures (see also figure 19). The light grey contours in the free stream in figure 17, in between the impinging wakes, correspond to background fluctuations.

Figure 18 shows a series of snapshots of the instantaneous velocity in the $y$-direction from Simulation III in a plane adjacent to the suction side surface. There is evidence of a turbulent spot, identified by the black ellipse, present in the snapshot that was taken at $t/P = 38.467$. In the subsequent snapshots the turbulent spot grows slightly in size as it is convected downstream and slowly merges with the turbulent region immediately upstream of the trailing edge. A similar series of snapshots, showing greyscale contours of the instantaneous temperature is shown in figure 24.

Figure 19 shows two sequential snapshots of vortical structures found along the pressure side of the blade in Simulation II. The locations where the wakes impinge are labelled 'W'. As in the simulations of flow in the T106 cascade with impinging wakes (Wu & Durbin 2001; Wissink 2003), longitudinal vortical structures are obtained along the pressure side. Compared to the T106 simulations, the structures obtained here are much thinner. This is a consequence of the relatively small vortical structures in the impinging wakes, which are responsible for inducing longitudinal vortical structures along the pressure side. The small vortical structures in the wake are formed by the interaction of the large vortical structures and the background fluctuations (see

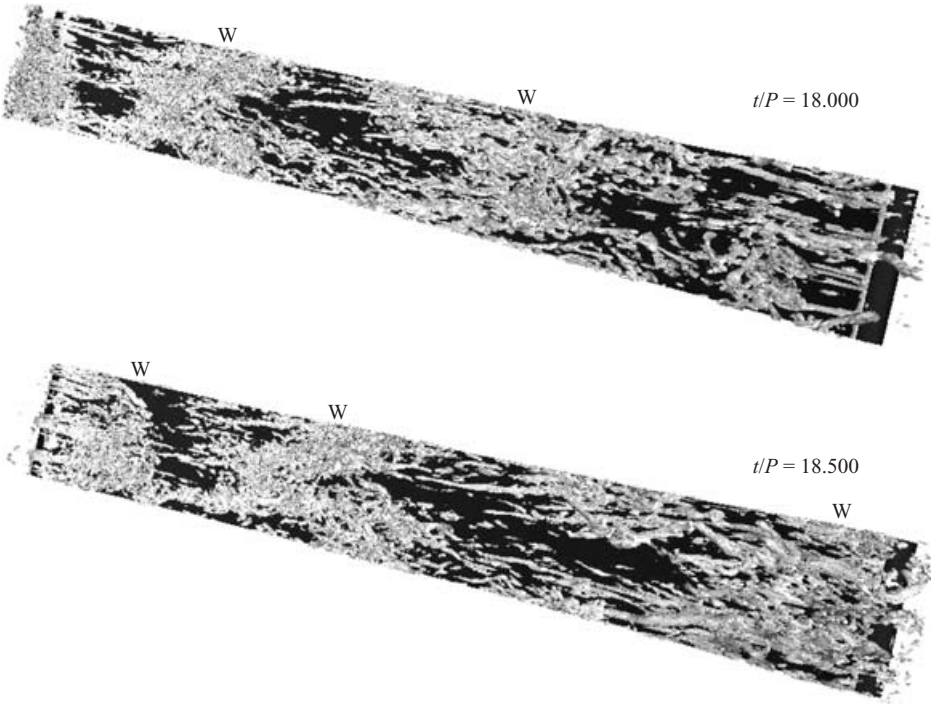


FIGURE 19. Simulation II: two snapshots showing vortical structures along the pressure side. The structures have been made visible using the $\lambda_2$-criterion of Jeong & Hussain (1995).

also Wissink & Rodi 2005). It is important to note that these longitudinal structures are not found to be present in the simulation without incoming wakes. Because the wakes are passively convected by the accelerating flow along the pressure side, the distance between two adjacent locations of impingement increases in the downstream direction.

As opposed to the structures in the FPG region of the suction side discussed above, the structures on the pressure side are formed as wakes actually impinge (at non-zero angle of attack) on the boundary layer. Compared to these, the lifetime of the structures observed along the FPG part of the suction side is relatively short. Indirect evidence of suction-side structures is given, for instance, in figure 28.

### 2.2. *Heat transfer*

As a dimensionless representation of the heat flux we use the local Nusselt number $Nu$, which, using $L$ as length-scale, is defined by

$$Nu = \frac{q_w}{T_0 - \alpha T_0}\frac{L}{k} = \frac{-1}{1-\alpha}\frac{\partial(\overline{T}/T_0)}{\partial(n/L)},$$

where $q_w$ is the heat-flux at the wall, $k$ is the thermal conductivity of the fluid, $\alpha$ is the ratio between the temperature of the outer flow and the temperature of the blade and $n$ is the wall-normal distance.

Note that the experimental results presented in Liu & Rodi (1994*b*) were made non-dimensional using $k = 0.0262\,\mathrm{mK}^{-1}$, which is the thermal conductivity of air at $T = 300\,\mathrm{K}$.

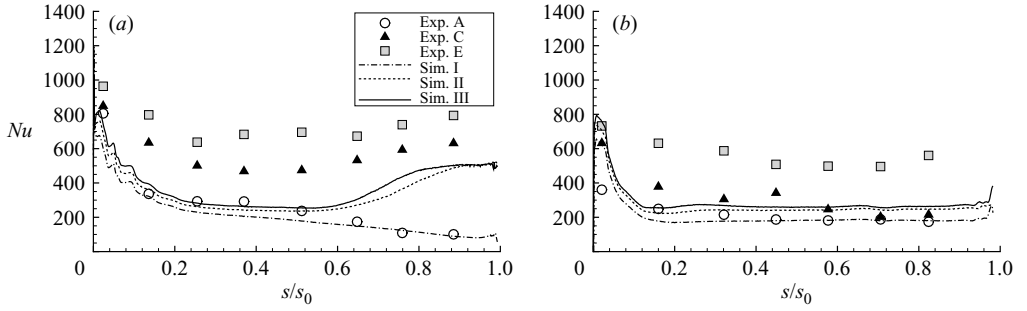


FIGURE 20. Time-averaged Nusselt number; comparison to experiment along both (*a*) the suction side and (*b*) the pressure side.

2.2.1. *Time-averaged statistics*

In figure 20, the distributions of the time-averaged Nusselt number, $Nu$, along the suction and pressure side obtained in Simulations I, II and III are compared with the experiments A, C and E, respectively. A direct comparison of figure 20 with figure 9 shows that, in general, the skin friction coefficient and the local Nusselt number are strongly correlated. Along the suction side, for the fully laminar case, Simulation I without wakes, the agreement with Experiment A is found to be very good. The peak value of $Nu$ near the leading edge is captured correctly and so is the decline of $Nu$ along the suction side. For the cases with wakes, the experiments (C and E) indicate a much weaker decay and an increase in $Nu$ from $s/s_0 \approx 0.5$, which is due to the wake-induced transition and the associated increase in heat transfer by turbulent fluctuations in the boundary layer. This increase is predicted correctly in Simulations II and III, as was to be expected from the predicted increase in friction coefficient in figure 9, but in the pre-transitional region upstream of $s/s_0 \approx 0.6$, the decline from the correctly predicted peak value near the leading edge is too strong, i.e. the measured increase in heat transfer level in this region was not reproduced in the simulations. There is some increase, approximately 20 % in Simulation II and 30 % in Simulation III, but this is much lower than the experimentally observed one.

Also along the pressure side, the agreement between Simulation I and Experiment A is very good over most of the blade. However, near the leading edge, there is a discrepancy: the peak value in Simulation I is similar to that on the suction side, which seems reasonable, whereas in the experiment the first measured value past the leading edge is substantially lower, which is hard to understand. For the situations with wakes, the experimental peak values are again much higher near the leading edge and are well reproduced in Simulations II and III. The decline of $Nu$ along the pressure side is then fairly well reproduced by Simulation II and over most of the blade a $Nu$ level is predicted which is about 30 % higher than that for simulation I without wakes, in fairly good agreement with Experiment C. This increase can be explained by the presence of longitudinal vortical structures induced by the impinging wakes that are observed along the pressure side of LPT blades as shown in figure 19. These structures promote the downwash of cool fluid from the free stream towards the blade and the upwash of hot fluid from the surface of the blade, as illustrated for Simulation III in figure 31. However, in spite of the doubled wake frequency and the higher background turbulence level as opposed to Simulation II, the heat transfer in Simulation III is only marginally higher than in Simulation II. On the other hand, in Experiment E, the heat transfer is considerably higher than in the other cases. In

the suction-side boundary layer of Simulation III, the maximum turbulent Prandtl number at any station is found to increase gradually from $Pr_T = 0.5$ at $s/s_0 = 0.2$ to approximately $Pr_T = 1$ in the turbulent region at the trailing edge.

From the above, it can be noted that the effect of passing wakes and background turbulence on the heat transfer is simulated in reasonable accord with the experiment in regions where the boundary layer is transitional or mildly turbulent. However, this is not the case in regions were the boundary layer is laminar, as in the pre-transitional regions on the suction side and on the pressure side especially for the case with larger wake frequency and background turbulence. There, the increase in 'laminar' heat transfer predicted by DNS is considerably smaller than observed in the experiments. In the pre-transitional regions on the suction side, the fluctuations in the boundary layer induced by the wakes and background turbulence have the correct average level in Simulation II *vis-á-vis* Experiment C and are even larger in Simulation III compared with Experiment E (see figure 8). Hence, the increase in laminar heat transfer as observed in the experiments is not only associated with the average level of the fluctuations in the boundary layer, but the spectral content of the disturbances impinging on the blade wall, i.e. the size of the eddies in the wakes, also has an important influence on this heat transfer. Therefore, the discrepancy between the simulations and the experiments regarding the increase in laminar heat transfer due to passing wakes and background turbulence is probably due to differences in the size of the impinging eddies carried by the wakes. The wake data provided by Wu & Durbin correspond to far wakes with comparatively small-scale structures whereas in the experiment, the wakes probably still carried some larger-scale fluctuations of the size of the wake width. It was observed in experiments on laminar heat transfer by Yardi & Sukhatme (1978) and Magari & LaGraff (1994) that it is the large scales that are most effective in increasing the heat transfer, whereas Kestin *et al.* (1961) and Junkhan & Serovy (1967) have shown that in order to obtain an increase in laminar heat transfer it is also necessary that the boundary-layer flow is accelerating (which happens to be the case in the present problem in the regions where the boundary layer remains laminar). According to Dullenkopf & Mayle (1995), free-stream fluctuations with an integral length scale $\Lambda$ that is approximately 10 times the boundary-layer thickness $\delta$ are most effective in increasing laminar heat transfer.

In our simulations, along the suction side, the thickness of the laminar part of the boundary layer varies between $\delta = 0.0040L$ at $s/s_0 = 0.10$ and $\delta = 0.0121L$ at $s/s_0 = 0.60$; along the pressure side, downstream of $s/s_0 = 0.10$, $\delta$ is always larger than $\delta = 0.0104L$. As can be seen from figure 26B, C and also from figure 29, the spanwise size of the impinging structures is about $0.02L - 0.03L$ which is comparable to the spanwise integral length scale of the impinging wakes and the background fluctuations. As this is considerably smaller than $10\delta$ in the entire laminar part of the blade's boundary layer downstream of $s/s_0 = 0.10$, it is understandable that there is no significant increase in laminar heat transfer triggered by impinging fluctuations from the outer flow. As noted before, in the experiment the distance the wake travels before reaching the leading-edge-plane of the turbine cascade was about 42 cylinder diameters. Consequently, the wakes entering the cascade still have near-wake character and are likely to carry significant structures with size of the order of the wake width, in which case eddies of size $\Lambda \approx 0.1L$, i.e. almost five times as large as in the numerical simulations, entered the cascade. According to the previous findings, these large coherent structures would be more effective in increasing the laminar heat transfer than the relatively small structures present in the artificial wakes entering in

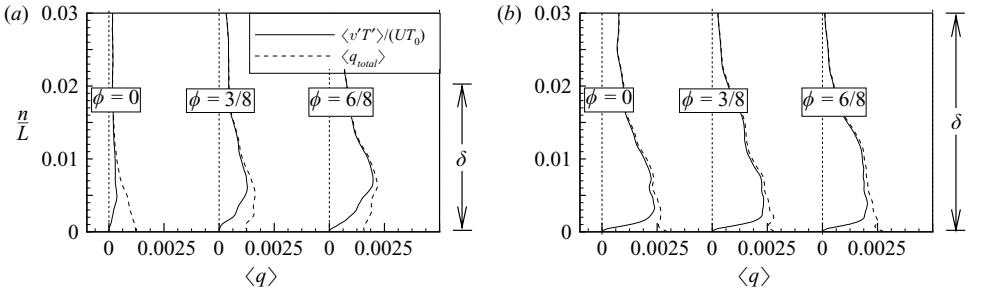


FIGURE 21. Simulation II: suction side: normal profiles at (*a*) $s/s_0 = 0.60$ and (*b*) $s/s_0 = 0.90$ of the phase-averaged wall-normal turbulent heat flux, $\langle v'T' \rangle / UT_0$ and the total heat flux $\langle q_{total} \rangle$. The profiles correspond to three phases $\phi = 0, 3/8, 6/8$.

the numerical simulations. However, in agreement with Dullenkopf & Mayle (1995), the influence of these smaller scales on transition is found to be correct.

2.2.2. *Phase-averaged statistics*

Figure 21 shows profiles of the phase-averaged wall-normal turbulent heat-flux $\langle v'T' \rangle$ and the wall-normal total heat flux

$$\langle q_{total} \rangle = \frac{\langle v'T' \rangle}{UT_0} - \left\langle \frac{1}{Pr\ Re} \frac{\partial (T/T_0)}{\partial (n/L)} \right\rangle$$

along the suction side of the blade in Simulation II at $s/s_0 = 0.60$ and $s/s_0 = 0.90$ for three phases (where $Re = UL/\nu$). Except in the lower part of the boundary layer, the turbulent heat-flux is found to be the dominant contributor to the total heat-flux. When approaching the surface, however, its contribution goes to zero. This indicates that the fluctuations promoting wall-normal heat transfer do not manage to penetrate the lower part of the boundary layer, which typically has strong shear. Still, as also witnessed by the snapshots – showing contours of the instantaneous temperature – in figure 26, the impinging disturbances do manage to transport some hot fluid from close to the surface of the blade towards the free stream, thereby increasing the turbulent heat flux. Compared to the profiles at $s/s_0 = 0.60$, the turbulent heat-flux profiles at $s/s_0 = 0.90$ can be seen to reach their maxima much closer to the blade's surface. This can be explained by the fact that at $s/s_0 = 0.90$, the boundary layer is intermittently turbulent. Consequently, small-scale turbulent motions play an important role in promoting wall-normal heat transfer, even relatively close to the surface of the blade. A clear phase-dependency of the heat-flux profiles can be observed at $s/s_0 = 0.60$. With the wake, also the location of the maximum turbulent heat-flux gradually approaches the blade's surface. At $s/s_0 = 0.90$, the phase-dependency of the profiles is rather small and the level of $\langle v'T' \rangle$ has increased inside the mildly turbulent boundary layer. The latter is reflected by an increase in the local Nusselt number.

The boundary layer along the pressure side remains laminar at all times. As a consequence, the level of the $\langle v'T' \rangle$-profiles and the $\langle q_{total} \rangle$-profiles (figure 22) is relatively small compared to the level of the corresponding profiles obtained in the mildly turbulent part of the suction-side boundary layer at $s/s_0 = 0.90$ (see figure 21). Also, the phase-dependency of the profiles along the pressure side at both locations $s/s_0 = 0.60$ and $s/s_0 = 0.90$ is almost negligible. The fact that the level of $\langle v'T' \rangle$ at both locations is comparable indicates that the local Nusselt number is also comparable,

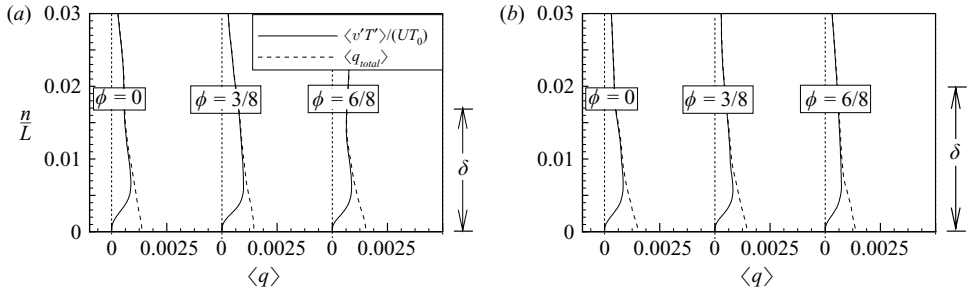


FIGURE 22. Simulation II: pressure side: normal profiles at (*a*) $s/s_0 = 0.60$ and (*b*) $s/s_0 = 0.90$ of the phase-averaged wall-normal turbulent heat flux, $\langle v'T' \rangle / UT_0$ and the total heat flux $\langle q_{total} \rangle$. The profiles correspond to three phases $\phi = 0, 3/8, 6/8$.

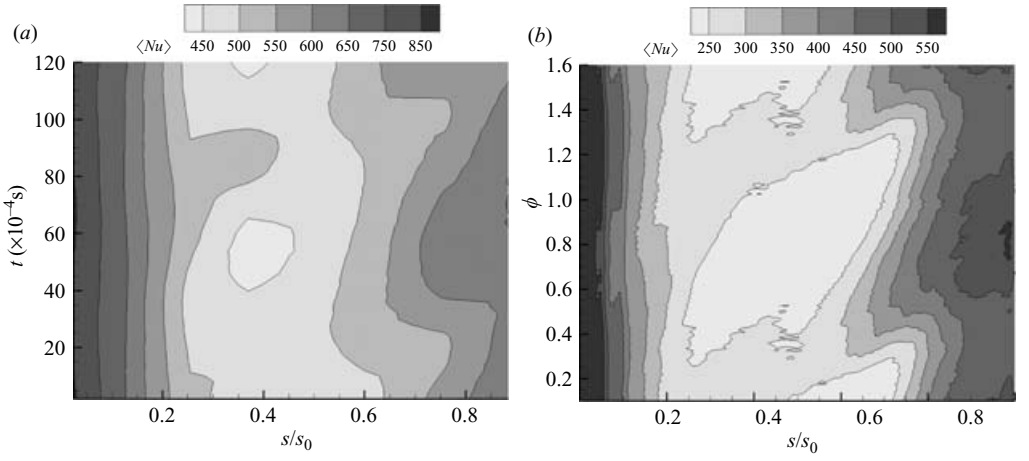


FIGURE 23. Space–time plot of the phase-averaged Nusselt number, $\langle Nu \rangle$, along the suction side as a function of the normalized surface-coordinate. (*a*) Experimental Case C, (*b*) Simulation II.

which is confirmed in figure 20 by the plateau in the mean $Nu$-signal along the pressure side downstream of $s/s_0 \approx 0.15$.

In figure 23, a comparison is shown of the phase-averaged Nusselt number $\langle Nu \rangle$ along the suction side of the blade between Experiment C and Simulation II. The local Nusselt number has been visualized using grey-scale contours in a space–time plot. Because of the large values of $Nu$ reached in the experiment, as compared to the DNS, it was necessary to employ different contour levels for each case. Both in the DNS and in the experiment a relatively low Nusselt number region is found around $s/s_0 = 0.4$. In the experiment, however, this region is much smaller than the region obtained in the numerical simulation. Also, as already discussed above, the Nusselt number in the pre-transitional region of the experiment is significantly larger than the Nusselt number obtained in the numerical simulation. Both plots show a phase-dependency in the magnitude of the Nusselt number downstream of $s/s_0 = 0.15$, which is especially clear in the APG region between $s/s_0 = 0.6$ and $s/s_0 = 0.8$.

Along the pressure side, the difference between the mean and the phase-averaged Nusselt number is never larger than 8.5 % so that the phase-dependency of $\langle Nu \rangle$ is only marginal.

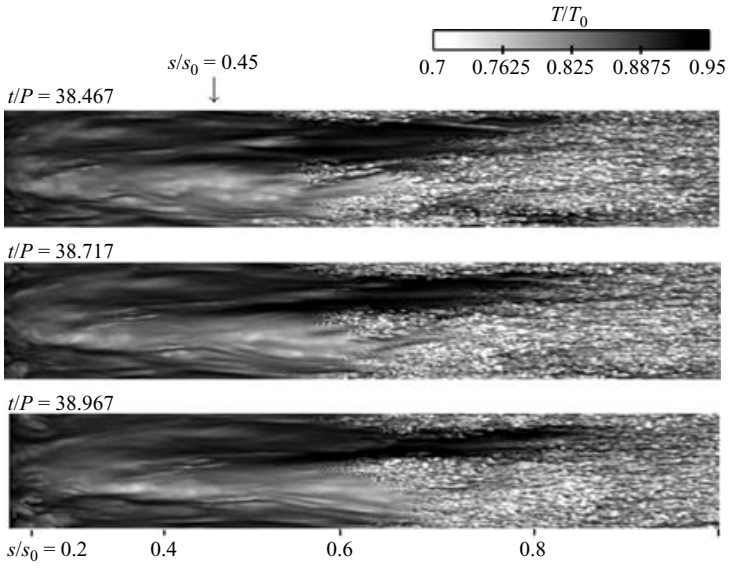


FIGURE 24. Simulation III: snapshots showing grey-scale contours of the instantaneous temperature at three instants in a plane at a distance of 0.18 %$L$ from the suction side of the blade (see also figure 18).

### 2.2.3. *Instantaneous temperature fields*

A series of three snapshots of Simulation III, showing grey-scale contours of the instantaneous temperature $T/T_0$ near the suction side, is shown in figure 24 at the same instants as the instantaneous vertical velocity contours plotted in figure 18. A comparison of the two figures illustrates the existence of a strong correlation between the distribution of velocity and temperature fluctuations which was also found in Wu & Durbin (2000). In the transitional region, the temperature distribution is rather fine-grained, while further upstream relatively large-scale fluctuations in the temperature can be observed, which give evidence that the impinging wakes affect the boundary layer not only in the adverse pressure gradient region, but also in the favourable pressure gradient region, where the wake's vortical structures are stretched and become aligned with the direction of flow.

As observed earlier, the accelerating flow causes the vorticity of the impinging vortical structures to become aligned with the direction of flow. Once present in the outer part of the boundary layer, their predominantly streamwise vorticity triggers vertical exchange of fluid. This exchange hardly contributes to $C_f$ or $\langle u'v' \rangle$ since the vorticity of the longitudinal structures is not found to significantly alter its streamwise orientation. This is opposed to hairpin vortices which are known to have a positive angle of 45° with the surface of the blade (see Pope 2000). The vertical exchange of fluid results in the formation of streaky structures illustrated in figure 18, see also Zaki & Durbin (2005).

Figure 25 shows the corresponding snapshots for the pressure side. Here, the structures resemble somewhat the structures observed in the pre-transitional region of the suction side. Compared to the latter, however, the lifetime of the pressure-side structures is significantly longer. The longitudinal structures present near the pressure side can be regarded as 'footprints' of the vortical structures contained in the impinging wakes (see for instance figure 19). Near the leading edge, the boundary

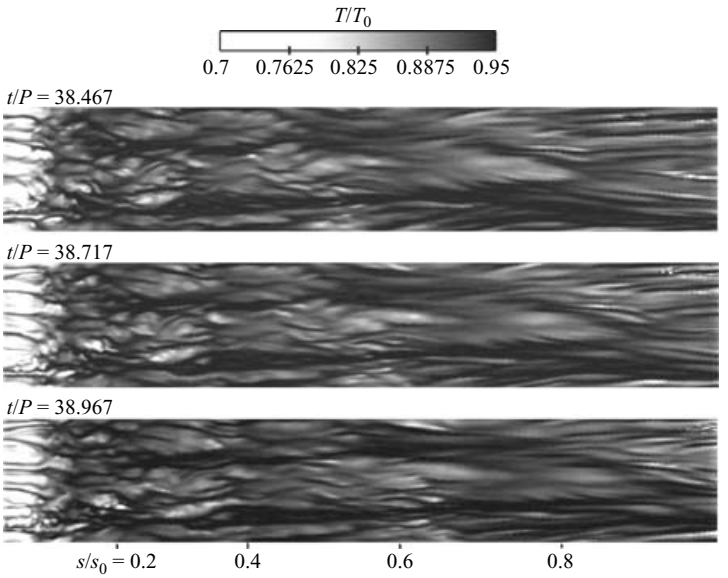


FIGURE 25. Simulation III: snapshots showing grey-scale contours of the instantaneous temperature at three instants in a plane at a distance of $0.18\,\%L$ from the pressure side of the blade.

layer is so thin, $\sim O(0.18\,\%L)$, that the plane considered is outside the boundary layer and the temperature contours show values which are typical for the free stream and, hence, are relatively light.

Figure 26 shows snapshots at $t/P = 15.033$ of the vector field of the instantaneous fluctuating velocity $||\boldsymbol{u}' = \boldsymbol{u} - \langle \boldsymbol{u} \rangle||$ and contours of the instantaneous temperature-field, $T/T_0$, in the cross-sections $s/s_0 = 0.05, 0.25, 0.45,\ 0.65, 0.85, 0.95$ of the suction-side boundary layer of the blade from Simulation II. The location of the wakes with respect to these cross-sections is identified in the upper graph showing contours of the magnitude of the instantaneous fluctuating velocity at mid-span, while at the far right, $\delta$ identifies the mean thickness of the boundary layer. In general, both wakes and background disturbances manage to introduce fluctuations into the upper part of the boundary layer and affect the local temperature distribution. In the APG region downstream of $s/s_0 = 0.60$, the boundary layer eventually undergoes by-pass transition – triggered by impinging disturbances – leading to an increase in heat transfer.

In the cross-sections in the pre-transitional FPG region upstream of $s/s_0 = 0.60$, concentrated streamwise vorticity – which is generated by the stretching of vortical structures – can be seen to impinge on the laminar boundary layer. The structures correspond to the vortical flow observed either in the free-stream or impinging on the boundary layer and promote the upwash of hot fluid away from the wall into the free stream as is shown clearly in the snapshots at $s/s_0 = 0.05$, $s/s_0 = 0.25$ and $s/s_0 = 0.45$. Further downstream, in the APG region the streamwise vorticity in the free stream becomes much less intense, while the vortices themselves are significantly larger. Still, we can see that the streamwise vortices do affect the boundary-layer flow and, consequently, also the heat transfer (see for instance the snapshot at $s/s_0 = 0.85$). At $s/s_0 = 0.95$, the boundary layer shows the presence of a turbulent spot at $z/L = 0.175$ giving evidence of by-pass transition. At both $s/s_0 = 0.085$ and

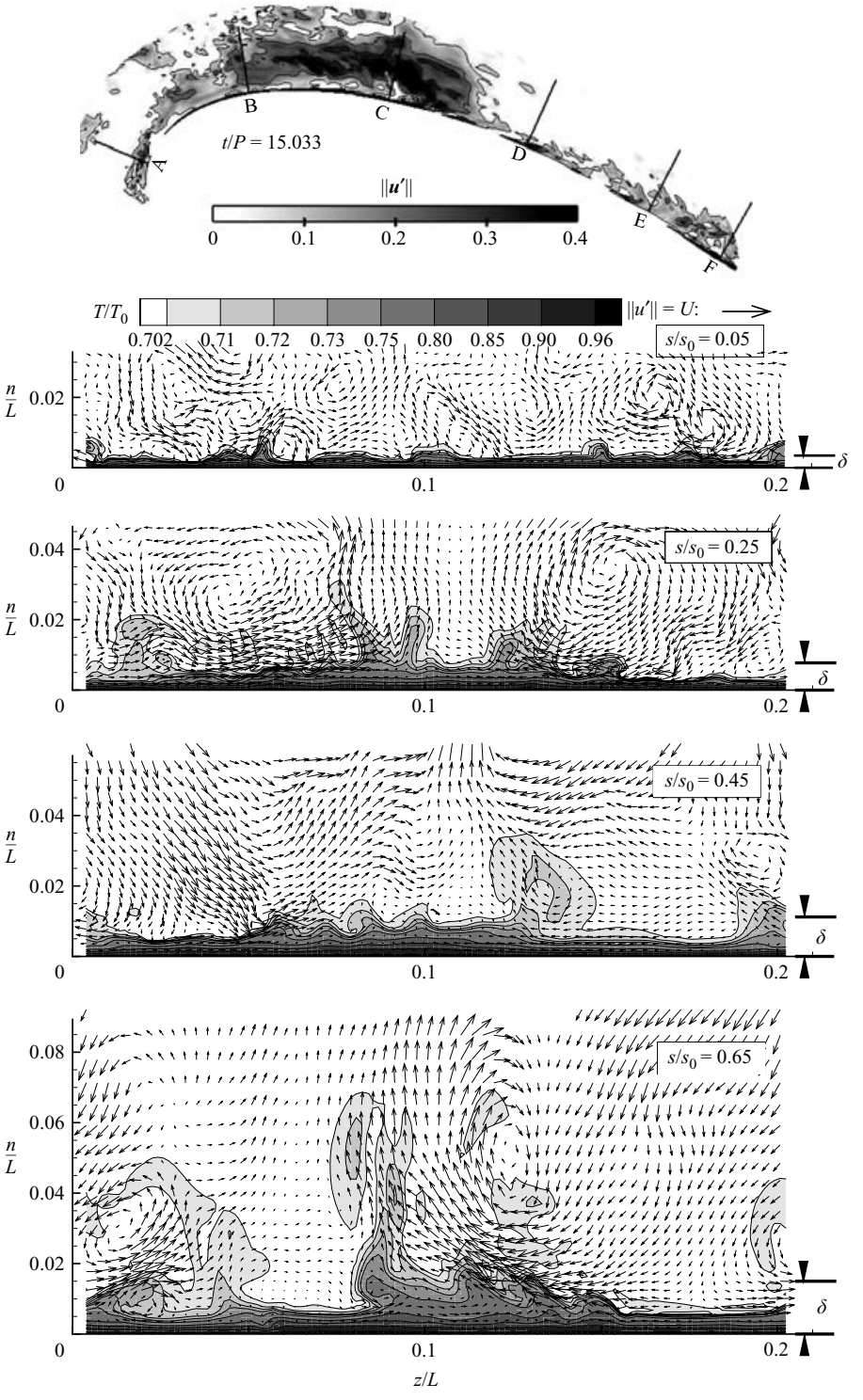


FIGURE 26. For caption see next page.

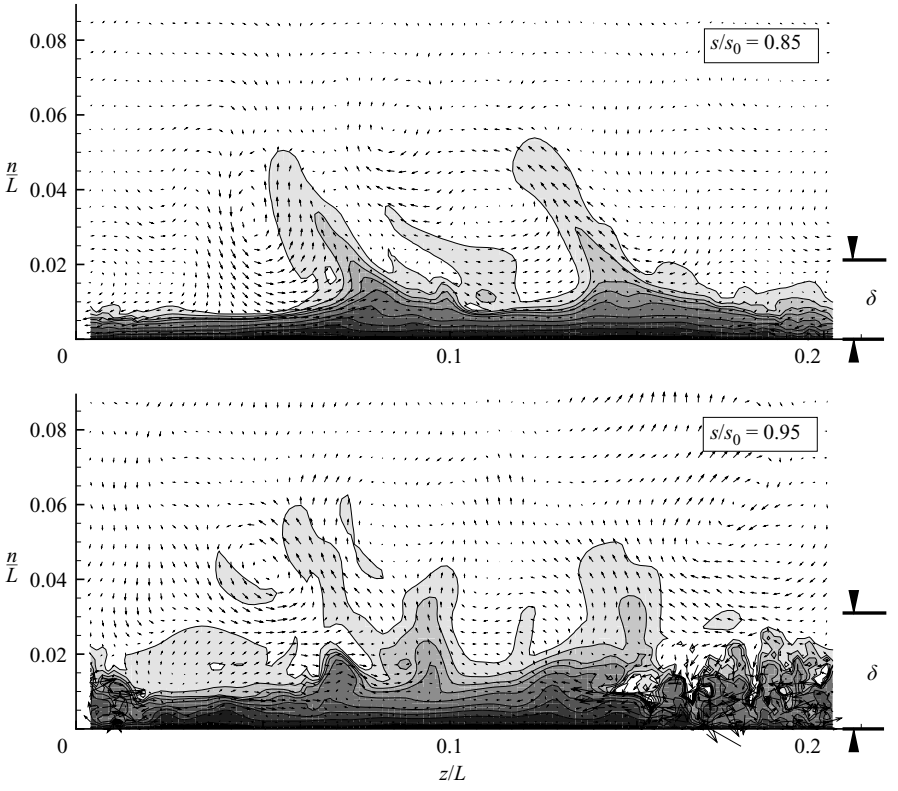


FIGURE 26. Simulation II: temperature contours $T/T_0$ and vector field of the fluctuating velocity in cross-sections of the suction-side boundary-layer at $t/P = 15.033$. The vector field shows vectors in every other grid point. The thickness of the boundary layer is identified by $\delta$. The snapshot of the fluctuating velocity magnitude at midspan displayed at the top is supplied to identify the location of wakes and other disturbances. The labels correspond to A: $s/s_0 = 0.05$, B: $s/s_0 = 0.25$, C: $s/s_0 = 0.45$, D: $s/s_0 = 0.65$, E: $s/s_0 = 0.85$, F: $s/s_0 = 0.95$

$s/s_0 = 0.95$, the flow is highly intermittent and the location of transition varies with the intensity of the impinging disturbances and thus with time. For instance, at $t/P = 20.00$ (not illustrated here) a turbulent spot is observed at $s/s_0 = 0.85$, while at $s/s_0 = 0.95$ almost the entire suction-side boundary layer has turned turbulent. Note that the above does not correspond to the picture in figure 18 which is for Simulation III.

In figure 27, the location of the wakes with respect to the cross-sections shown in figures 28–32 is identified using contours of the fluctuating velocity magnitude from Simulation III. In this case of high wake-frequency, disturbances are almost continuously impinging on the blade's boundary layer. Still, it is possible to identify individual wakes by a slight local increase in fluctuations. At location 'A' ($s/s_0 = 0.05$), for instance, no wake is observed to be impinging such that the local free-stream flow contains only a few disturbances. For $n/L < 0.025$, though, fluctuations still persist and the sequence of snapshots displayed in figure 28 – showing grey-scale contours of $T/T_0$ together with the vector field of the fluctuating velocity at $t/P = 38.467$, $t/P = 38.500$ and $t/P = 38.533$ in the cross-section at $s/s_0 = 0.05$ – makes it possible to track their short-time evolution. Some of the structures in figure 28, such as the large mushroom-like structure at $z/L \approx 0.175$, are present in all three snapshots. Compared

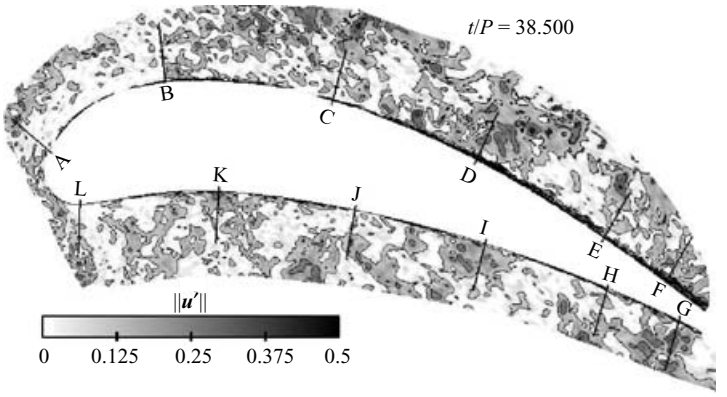


FIGURE 27. Simulation III: contours of the fluctuating velocity magnitude at midspan. The labels A, . . . ,L identify the locations of the cross-sections plotted in figures 28, 30 and 31.

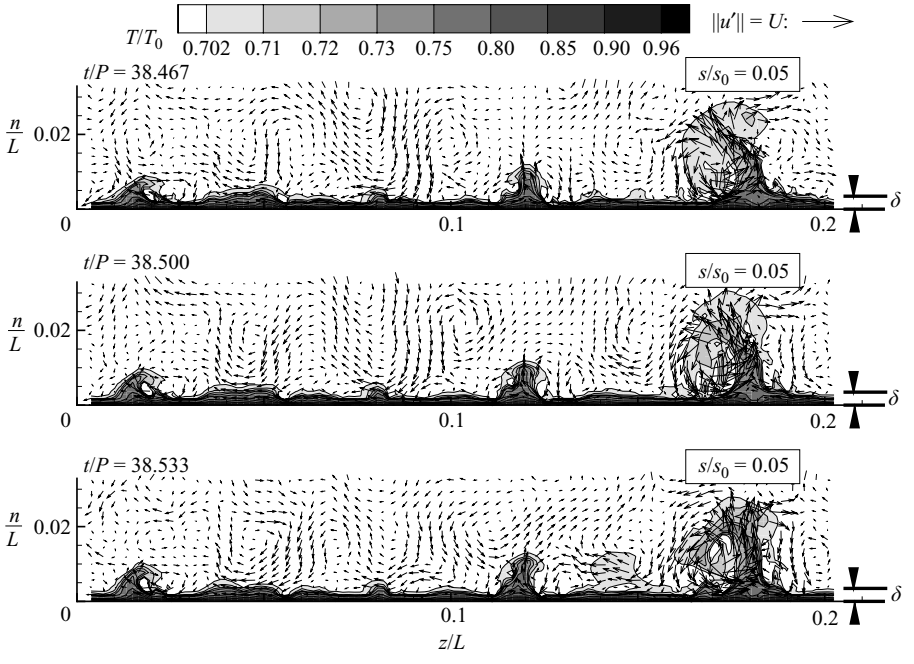


FIGURE 28. Simulation III: contours of the temperature $T/T_0$ and the vector field of the fluctuating velocity in cross-sections of the suction-side boundary-layer. Vectors are shown in every other grid point. At $s/s_0 = 0.05$, snapshots are shown at $t/P = 38.467$, $t/P = 38.500$ and at $t/P = 38.533$. The thickness of the boundary layer is identified by $\delta$. The locations of the wakes, background fluctuations and the cross sections are identified in figure 27, where $s/s_0 = 0.05$ corresponds to label $A$.

to their spanwise extent, the streamwise extent of these structures is relatively long. For instance, the mushroom is convected downstream with velocity $1.7U$ (determined from the statistics gathered), such that the streamwise extent of the corresponding vortex is at least $0.112L$ which is five times its spanwise extent. Other structures have a streamwise extent that is at least ten times as large as their spanwise extent. All of this gives evidence of the vortex-stretching in the FPG region discussed earlier. Note

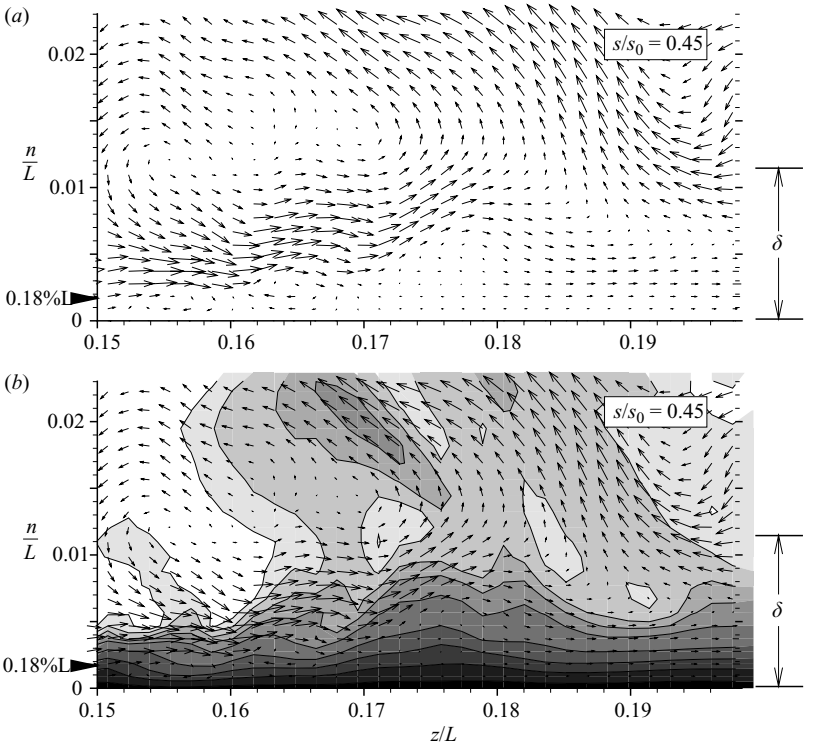


FIGURE 29. Simulation III: snapshot of the vector field of the fluctuating velocity at $t/P = 38.467$ – in one graph combined with contours of the the temperature $T/T_0$ – in part of the cross-section at $s/s_0 = 0.45$ of the suction-side boundary-layer. The locations of the wakes, background fluctuations and the cross-section are identified in figure 27, where $s/s_0 = 0.45$ corresponds to label C. The mean thickness of the boundary layer is identified by $\delta$ and the legend of $T/T_0$ is given in figure 28.

that most structures shown in figures 26 and 28 have a typical spanwise extent of approximately $0.02L$, which virtually matches the integral length scales $\Lambda = 0.019L$ of the background fluctuations and is also similar to the spanwise integral length scale $\Lambda = 0.027L$ in the wakes as determined at the inlet plane (see figure 2).

Figure 29 shows an enlarged snapshot of $u'$ and contours of the temperature in a part of the cross-section at $s/s_0 = 0.45$, which – as witnessed by the top pictures in figures 18 and 24 – is located in the pre-transitional region. The figure clearly shows re-circulating flow that impinges on the outer part of the boundary layer and induces relatively weak secondary re-circulation, with opposite rotation, further down. Though the relatively strong fluctuations are not able to penetrate very deep into the boundary layer, they still manage to promote the mixing of hot and cold fluid moderately, leading to an increase in $Nu$ of about 30 % as compared to Simulation I (see also figure 20).

Both parts in figure 30 show a snapshot of a detailed vector plot of the fluctuating velocity field at $t/P = 38.467$ in part of the cross-section at $s/s_0 = 0.95$ of the turbulent boundary-layer from Simulation III (see also figure 24). In figure 30($b$), the vector field is combined with contours of the instantaneous temperature. The scales of the vector field and the temperature contours are identical to the scales employed in figure 28. The vector plot shows the presence of intense small-scale streamwise

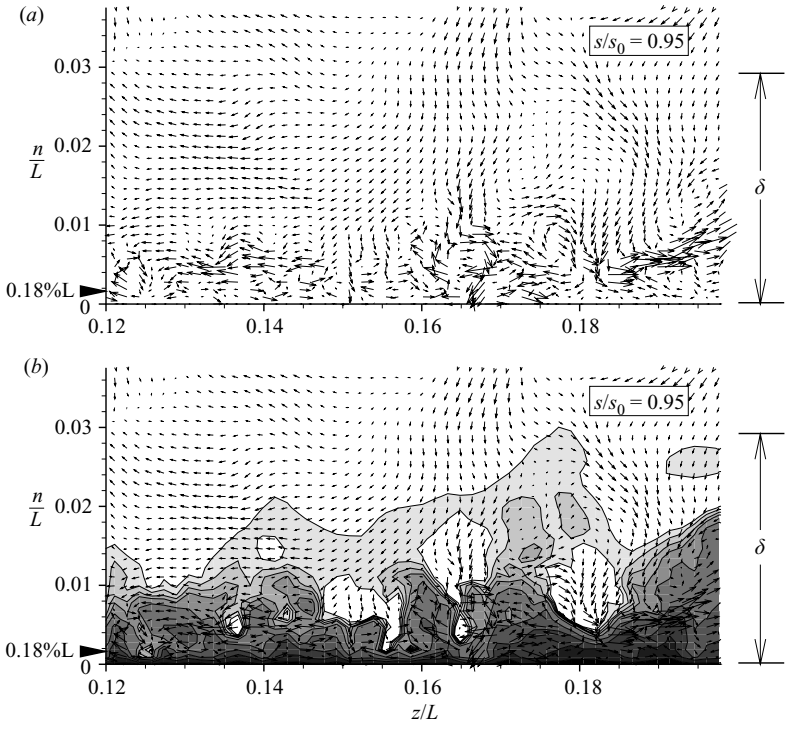


FIGURE 30. Simulation III: snapshot of the vector field of the fluctuating velocity at $t/P = 38.467$ – in one graph combined with contours of the the temperature $T/T_0$ – in part of the cross-section at $s/s_0 = 0.95$ of the suction-side boundary-layer. The locations of the wakes, background fluctuations and the cross-section are identified in figure 27, where $s/s_0 = 0.95$ corresponds to label F. The mean thickness of the boundary layer is identified by $\delta$ and the legend of $T/T_0$ is given in figure 28.

vorticity. Apart from a very thin layer close to the surface of the blade – corresponding approximately to the viscous sublayer – the temperature contours indicate that the near-wall turbulence efficiently promotes the mixing of hot and cold fluid, thereby significantly increasing the heat transfer (see also figure 20).

Figure 31 shows snapshots at $t/P = 38.467$ of the instantaneous temperature field, $T/T_0$, and vectors of the fluctuating velocity field in the cross-sections $s/s_0 = 0.05$, 0.25, 0.45, 0.65, 0.85, 0.95 on the pressure side of the blade from Simulation III (see also figure 25). The longitudinal streamwise vortical structures adjacent to the pressure side are identified by streamwise rotation – both inside and in the immediate proximity of the boundary layer – which is clearly visible in the cross-sections at $s/s_0 = 0.05, \ldots, 0.65$. Farther downstream, this rotation is more difficult to detect, because it is associated with streamwise vortices with a larger spanwise size. For instance, a large vortex with a spanwise size of approximately $0.08L$ – sweeping hot fluid from the surface of the blade into the free-stream – is observed at $s/s_0 = 0.95$. The snapshots suggest an intense mixing of hot and cold fluid near the blade. Compared to Simulation II, where the free-stream fluctuations are more moderate, however, this mixing is not found to lead to a drastic increase in heat transfer from the blade towards the free stream, as can be seen in figure 20.

Figure 32, finally, shows a close-up of the fluctuating velocity-field snapshot at $t/P = 38.467$ in the cross-section at $s/s_0 = 0.65$ on the pressure-side from Simulation III.

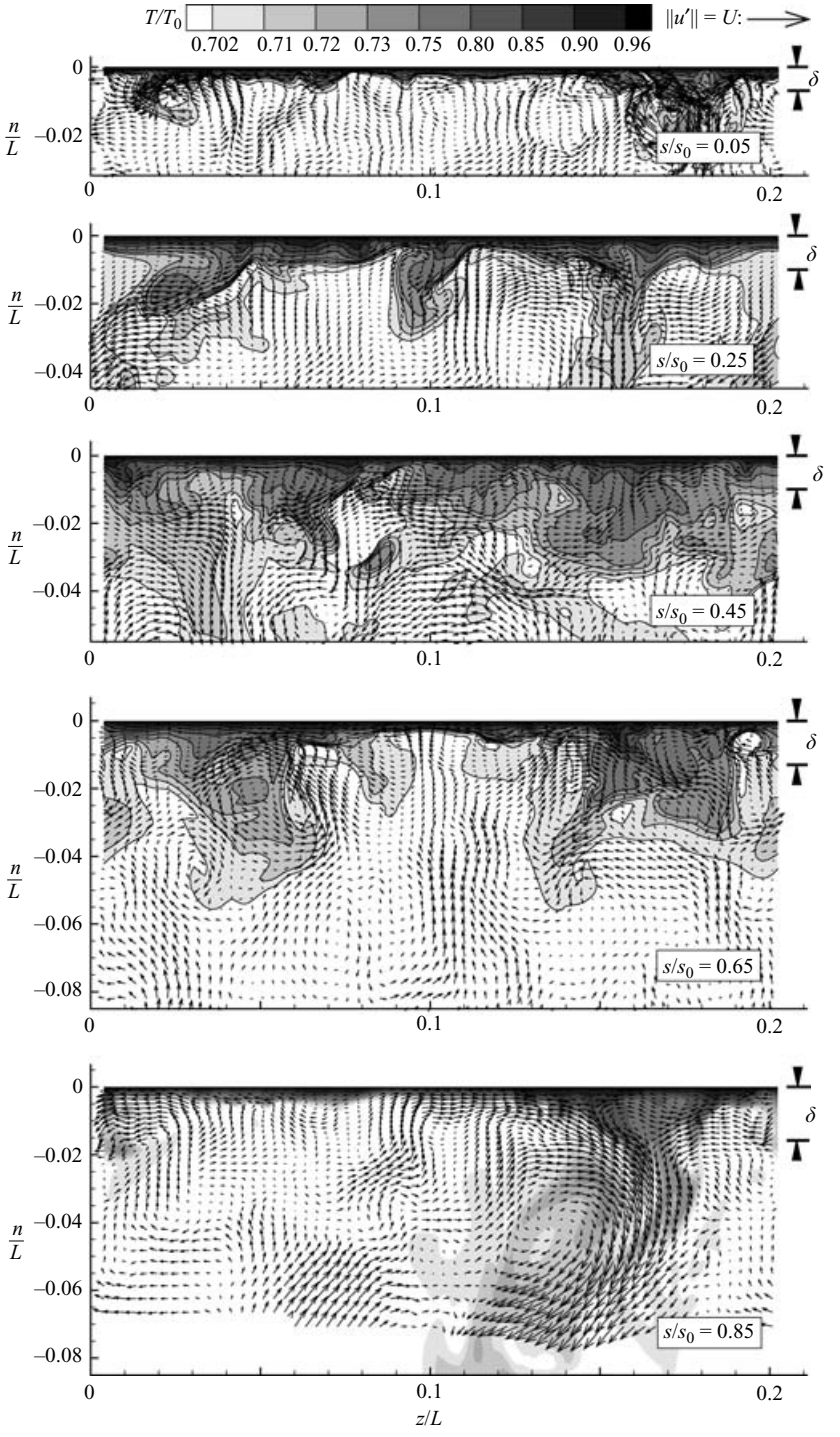


FIGURE 31. For caption see facing page.

The detailed vector plot clearly shows the presence of small-scale rotating flow inside the boundary layer. Both the rotating flow inside the boundary layer and the larger-scale re-circulating flow observed immediately outside of the boundary layer (see

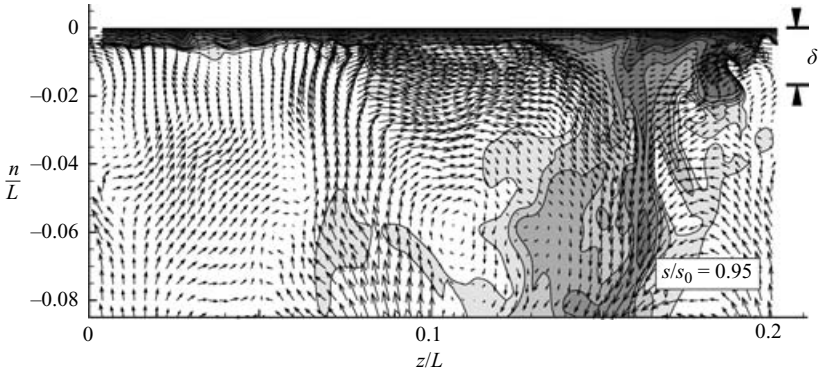


FIGURE 31. Simulation III: contours of the temperature field $T/T_0$ and vector field of the fluctuating velocity in cross-sections of the pressure-side boundary-layer at $t/P = 38.467$. Vectors are shown in every other grid point. The thickness of the boundary layer is identified by $\delta$. The locations of the wakes, background fluctuations and the cross-sections are identified in figure 27, where the labels correspond to L: $s/s_0 = 0.05$, K: $s/s_0 = 0.25$, J: $s/s_0 = 0.45$, I: $s/s_0 = 0.65$, H: $s/s_0 = 0.85$, G: $s/s_0 = 0.95$

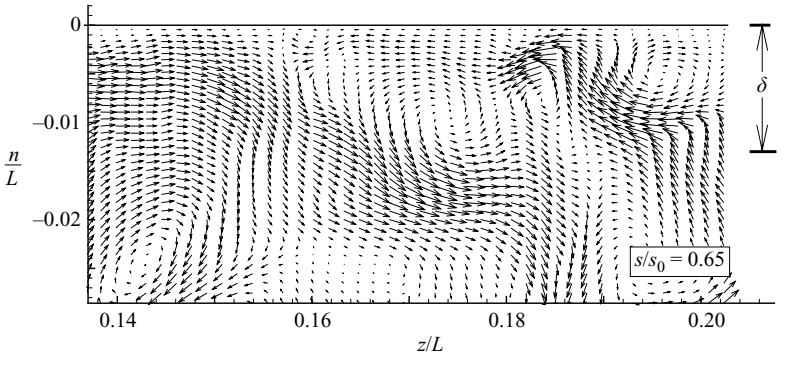


FIGURE 32. Simulation III: snapshot at $t/P = 38.467$ showing a detail of the vector field of the fluctuating velocity in the cross-section of the pressure-side boundary-layer at $s/s_0 = 0.65$. The thickness of the boundary layer is identified by $\delta$. The locations of the wakes, background fluctuations and the cross-section are identified by label I in figure 27.

figure 31) correspond to the longitudinal vortical structures shown in figure 19. As observed earlier along the suction side (see figure 28), again the typical spanwise extent of the structures observed along the pressure side in figure 32 approximately matches the integral length-scale of the background fluctuations $\Lambda = 0.019L$ and the spanwise integral length scale $\Lambda = 0.027L$ of the wakes, both determined at the inlet plane at $x/L = -0.50$ (see figure 2).

## 3. Discussion and conclusions

Direct numerical simulations of flow and heat transfer in a turbine cascade with and without oncoming wakes and background fluctuations have been performed. The computational domain was selected in accordance with a simplified version of the experimental set-up used by Liu & Rodi (1994*b*). In the simulations, the curvature of the squirrel cage on which the wake-generating cylinders were mounted was ignored and the distance between two adjacent cylinders, $D_{cyl}$, was slightly adjusted such

that $D_{cyl}$ became an integer divider of the pitch between blades, making it possible to employ periodic boundary conditions in the pitch-wise direction. Furthermore, the disturbances generated by the cylinders moving upwards in the upstream half of the cage were modelled by introducing background fluctuations at the inlet of the computational domain. The measured level of the background fluctuations was rather difficult to obtain, especially in Simulation III where, to complicate matters, the artificial wakes introduced at the inlet plane were found to have merged by the time they arrived at the first measurement station ($x/L = -0.20$). A perfect match of the experimental values at that station was only achieved in Simulation II with the help of a series of large-eddy simulations. In Simulation I, no background fluctuations were added while the level of background fluctuations added in Simulation III was found to be too large for a perfect match with Experiment E.

In all simulations, the wall static-pressure coefficient was found to be in very good agreement with experiment. Because of the absence of free-stream fluctuations in Simulation I, compared to Experiment A, only very minor streamwise fluctuations were obtained on the suction-side boundary-layer. In Simulation II, however, the good match with the experimental *Tu*-level resulted in a very good agreement with Experiment C with regard to the wall-parallel flow in the suction-side's boundary-layer and its r.m.s.-values. As a result of the large *Tu*-level introduced at the inlet of Simulation III, the r.m.s.-values of the streamwise velocity near the suction side were found to be significantly larger than those measured in Experiment E.

In all simulations, the flow along the pressure side was found to remain laminar at all times. In the presence of the periodically incoming wakes, in Simulations II and III, longitudinal streamwise vortical structures were detected adjacent to the pressure side. These structures were observed earlier in the DNSs of flow with incoming wakes in a T106 LPT cascade performed by Wu & Durbin (2001) and Wissink (2003).

While in Simulation I the boundary-layer flow along the suction side remained completely laminar, in Simulation II and III the impinging free-stream fluctuations were found to trigger by-pass transition in the adverse pressure gradient region downstream of $s/s_0 = 0.60$. Compared to Simulation II, in Simulation III the onset of transition was located slightly farther upstream, caused by the stronger triggering of boundary-layer flow instabilities.

As observed previously (e.g. Wu & Durbin 2001; Wissink 2003), kinetic energy was found to be produced at the apex of the deformed wakes, where the direction of compression is aligned with the axis of the wake. The strong stretching of free-stream vortical structures by the mean flow adjacent to the suction side immediately downstream of the leading edge, forces the axes of these vortices to align with the flow-direction, virtually parallel to the surface of the blade. As a result, along the FPG region of the suction side, longitudinal streamwise vortices are observed, which impinge on the suction-side boundary-layer. Compared to the similar longitudinal vortices observed along the pressure side, which have a rather long life-time because of the low-convection speed, the vortices along the suction side are convected with much higher speed. As a result, no accumulation of longitudinal structures near the suction side is observed.

In the experiments, the free-stream fluctuations were observed to be able to significantly increase heat transfer along the pre-transitional part of the suction side and, in Experiment E, also along the entire pressure side. Compared to this, the free-stream fluctuations in the numerical simulations were only able to increase heat transfer on the pressure side by approximately 30 %. This increase was mainly due to the exchange of hot fluid from the surface of the blade and cold fluid from the free

stream by the longitudinal streamwise vortical structures which were triggered by the impinging wakes. Along the suction side, the simulations showed an increase in heat transfer comparable to that found in the experiments only in the region where the boundary-layer flow undergoes transition. In the pre-transitional still laminar FPG region farther upstream, compared to the simulation without free-stream fluctuations, heat transfer was found to be increased by approximately 20–30 %, compared to an increase in this region of 100 % in Experiment C and an increase of around 200 % in Experiment E. The mechanism behind this increase in laminar heat transfer on the suction side is very similar to the mechanism observed along the pressure side: streamwise vorticity, introduced into the boundary layer, promotes the exchange of hot low-speed fluid near the blade with cold high-speed fluid from the free stream. As a result, low-speed and high speed streaks are formed in the FPG part of the boundary layer.

The reasons for the observed differences in 'laminar' heat transfer in the presence of free-stream fluctuations between experiments and DNSs cannot be fully clarified but – leaving aside possible experimental errors – these differences are believed to be mainly a consequence of the different spectral contents of the respective free-stream fluctuations. Dullenkopf & Mayle (1995) have shown that free-stream fluctuations with an integral length scale of $\Lambda \approx 10\delta$, where $\delta$ is the boundary-layer thickness, are particularly effective in increasing laminar heat transfer. In our simulations, the length scale of the free-stream fluctuations was found to be too small – by a factor of about 5 – to meet this criterion. In the experiments, there is unfortunately no information on the spectral contents of the wakes, which probably still had near-field character and, hence, contained larger vortical structures than the artificial wakes with a far-field character which were present in the numerical simulations. This could explain the large effect on heat transfer observed in the experiments. The inflow conditions employed in the DNS are not identical to the inflow conditions in the experiments, as in this and also in some other respects, the DNS results should be regarded in their own right.

Future work should address the dependence of laminar heat transfer on the integral length scale of the free-stream fluctuations. Also, the importance of streamwise vortices – generated by vortex-stretching of free-stream vorticity in the FPG region – in relation to the formation of streaks must be clarified.

The authors would like to thank the German Research Foundation (DFG) for funding this project and the steering committee of the Super Computing Facilities in Bavaria (HLRB) for granting computing time on the Hitachi SR8000-F1 at the Leibniz Computing Centre (LRZ) in Munich. We would also like to thank Xiaohua Wu and Paul Durbin of Standford University for kindly making the artificial wake data available.

## REFERENCES

Breuer, M. & Rodi, W. 1996 Large eddy simulation for complex turbulent flows of practical interest. In *Flow Simulation with High Performance Computers II*. Notes on Numerical Fluid Mechanics, vol. 52, pp. 258–274. Vieweg, Braunschweig.

Cho, N.-H., Liu, X., Rodi, W. & Schönung, B. 1993 Calculation of wake-induced unsteady flow in a turbine cascade. *Trans. ASME J. Turbomachinery* **115**, 675–686.

Comte-Bellot, G. & Corrsin, S. 1971 Simple Eulerian time correlations of full and narrow band velocity signals in grid-generated turbulence. *J. Fluid. Mech.* **48**, 273–337.

Dullenkopf, K. & Mayle, R. E. 1994 The effects of incident turbulence and moving wakes on laminar heat transfer in gas turbines. *Trans. ASME J. Turbomachinery* **116**, 23–28.

Dullenkopf, K. & Mayle, R. E. 1995 An Account of Free-Stream-Turbulence Length Scale on Laminar Heat Transfer. *ASME J. Turbomachinery* **117**, 401–406.

Dullenkopf, K., Schulz, A. & Wittig, S. 1991 The effect of incident wake conditions on the mean heat transfer of an airfoil. *Trans. ASME J. Turbomachinery* **113**, 412–418.

Edmunds, R., Jennions, I. K., Bohn, D. & Gier, J. 1999 The computation of adjacent blade-row effects in a 1.5-stage axial flow turbine. *Trans. ASME J. Turbomachinery* **121**, 1–10.

Germano, M. & Piomelli, U. & Moin, P. & Cabot, W. H. 1991 A dynamic subgrid-scale eddy viscosity model. *Phys. Fluids* A **3**, 1760–1765.

Hsu, K. & Lee, L. 1991 A numerical technique for two-dimensional grid generation with grid control at the boundaries. *J. Comput. Phys.* **96**, 451–469.

Hummel, F. 2002 Wake–wake interaction and its potential for clocking in a transonic high-pressure turbine. *Trans. ASME J. Turbomachinery* **124**, 69–76.

Jeong, J. & Hussain, F. 1995 On the identification of a vortex. *J. Fluid. Mech.* **285**, 69–94.

Jeschke, P. & Beer, H. 2001 Longitudinal vortices in a laminar natural convection boundary layer flow on an inclined flat plate and their influence on heat transfer. *J. Fluid. Mech.* **432**, 313–339.

Junkhan, G. H. & Serovy, G. K. 1967 Effects of free-stream turbulence and pressure-gradient on flat plate boundary layer velocity profiles and on heat transfer. *Trans. ASME* C: *J. Heat Transfer* **89**, 169–176.

Kalitzin, G., Wu, X. & Durbin, P. A. 2003 DNS of fully turbulent flow in a LPT passage. *Intl J. Heat Fluid Flow* **24**, 636–644.

Kestin, J., Maeder, P. F. & Wang, H. E. 1961 Influence of turbulence on heat transfer of heat from plates with and without a pressure gradient. *Intl J. Heat Mass Transfer* **3**, 133–154.

Lardeau, S. & Leschziner, M. A. 2004 Unsteady Reynolds-averaged Navier–Stokes computations of transitional wake/blade interaction. *AIAA J.* **42**, 1559–1571.

Lilly, D. K. 1992 A proposed modification of the Germano subgrid-scale closure method. *Phys. Fluids* A **4**, 633–635.

Liu, X. & Rodi, W. 1991 Experiments on transitional boundary layers with wake-induced unsteadiness. *J. Fluid Mech.* **231**, 229–256.

Liu, X. & Rodi, W. 1994*a* Velocity measurements in wake-induced unsteady flow in a linear turbine cascade. *Exps. Fluids* **17**, 45–58.

Liu, X. & Rodi, W. 1994*b* Surface pressure and heat transfer measurements in a turbine cascade with unsteady oncoming wakes. *Exps. Fluids* **17**, 171–178.

Magari, P. J. & LaGraff, L. E. 1994 Wake-induced unsteady stagnation-region heat transfer measurements. *Trans ASME J. Turbomachinery* **116**, 29–38.

Michelassi, V., Martelli, F., Dénos, R., Arts, T. & Sieverding, C. H. 1999 Unsteady heat transfer in stator–rotor interaction by two-equation turbulence model. *Trans. ASME J. Turbomachinery* **121**, 436–447.

Michelassi, V., Wissink, J. G. & Rodi, W. 2002 Analysis of DNS and LES of flow in a low-pressure turbine cascade with incoming wakes and comparison with experiments. *Flow Turb. Combust.* **69**, 295–329.

Pope, S. B. 2000 *Turbulent Flows*. Cambridge University Press.

Raverdy, B., Mary, I., Sagaut, P. & Liamis, N. 2003 High-resolution large-eddy simulation of flow around low-pressure turbine blade. *AIAA J.* **41**, 390–397.

Rhie, C. M. & Chow, W. L. 1983 Numerical study of the turbulent flow past an airfoil with trailing edge separation. *AIAA J.* **21**, 1525–1532.

Rogers, M. M. 2002 The evolution of strained turbulent plane wakes. *J. Fluid Mech.* **463**, 53–120.

Schobeiri, M. T., Pappu, K. & Wright, L. 1995 Experimental study of the unsteady boundary layer behavior on a turbine cascade. *ASME Paper* 95-GT-435, presented at the International Gas Turbine and Aero-Engine Congress and Exposition, Houston, Texas, June 5–8.

Schulte, W. & Hodson, H. P. 1998 Unsteady wake-induced boundary layer transition in high lift LP turbines. *Trans. ASME J. Turbomachinery* **120**, 28–35.

Stadtmüller, P. & Fottner, L. 2001 A test case for the numerical investigation of wake passing effects on a highly loaded LP turbine cascade blade. *ASME Paper* 1001-GT-311.

Wissink, J. G. 2003 DNS of separating, low Reynolds number flow in a turbine cascade with incoming wakes. *Intl J. Heat Fluid Flow* **24**, 626–635.

Wissink, J. G. & Rodi, W. 2005 LES of background fluctuations interacting with periodically incoming wakes in a turbine cascade. In *Proceedings of Direct and Large-Eddy Simulation VI* (ed. R. Friedrich, B. J. Geurts & O. Métais). Springer.

Wittig, S., Schulz, A., Bauer, H. J. & Sill, K. H. 1985 Effects of wakes on heat transfer in gas turbine cascades. *AGARD CP* **390**, 6-1–6-13.

Wu, X. & Durbin, P. A. 2000 Numerical simulation of heat transfer in a transitional boundary layer with passing wakes. *Trans. ASME J. Heat Transfer* **122**, 248–257.

Wu, X. & Durbin, P. A. 2001 Evidence of longitudinal vortices evolved from distorted wakes in a turbine passage. *J. Fluid Mech.* **446**, 199–228.

Wu, X., Jacobs R. G., Hunt, J. C. R. & Durbin, P. A. 1999 Simulation of boundary layer transition induced by periodically passing wakes. *J. Fluid Mech.* **398**, 109–153.

Yardi, N. R. & Sukhatme, S. P. 1978 Effect of turbulence intensity and integral length scale of a turbulent free stream on forced convection heat transfer from a circular cylinder in cross flow. *Proc. 6th Intl Heat Transfer Conference* Toronto, Canada, vol. 5, FC(b)-29, pp. 347–352.

Zaki, T. A. & Durbin, P. A. 2005 Mode interaction and the bypass route to transition. *J. Fluid Mech.* **531**, 85–111.